

See discussions, stats, and author profiles for this publication at: <https://www.researchgate.net/publication/233672669>

Numerical Calculations of the Quantum States in Semiconductor Nanostructures

Article *in* Journal of Computational and Theoretical Nanoscience · February 2010

DOI: 10.1166/jctn.2010.1380

CITATIONS

24

READS

174

2 authors:



Marcos H. Degani
University of Campinas

112 PUBLICATIONS 1,541 CITATIONS

[SEE PROFILE](#)



Marcelo Maialle
University of Campinas

58 PUBLICATIONS 1,070 CITATIONS

[SEE PROFILE](#)

Numerical Calculations of the Quantum States in Semiconductor Nanostructures

Marcos H. Degani^{1,*} and Marcelo Z. Maialle²

¹Haras Degani, Av. Fioravante Piovani 1000, Itatiba-SP, 13257-700, Brazil

²Liceu Vivere, R. Duque de Caxias Norte 550, Pirassununga-SP, 13635-000, Brazil

In this review we describe the use of a powerful numerical tool to obtain quantum states of semiconductor nanostructures. A detailed account of the numerical method is given and the method is applied to solve the Schrödinger equation for several semiconductor systems within the effective mass approximation. The variety of systems investigated shows how flexible and effective the method is. The scheme for the calculation of the eigenvalues and eigenvectors is a modified version of a split-operator approach to propagate the wave functions by infinitesimal time steps, applied both in real and imaginary time propagations. Interesting aspects in this modified approach are the use of real space coordinates, time propagation in real and imaginary domains, the treatment of excited states as well as of systems with interacting particles.

Keywords: Computational Techniques, Semiconductor Nanostructures, Excitons, Trions.

CONTENTS

1. Introduction	454
2. Formulation of the Method	455
2.1. Real-Time Evolution of the Wave Function: General Formulation	456
2.2. Imaginary-Time Propagation: Energy Spectrum	457
2.3. Band Structure of Periodic Systems	458
2.4. Higher Spatial Dimensions and Many Particles	458
2.5. Self-Consistent Potentials	459
3. Applications of the Method to Low-Dimensional Semiconductor Structures	460
3.1. The Stark Ladder Problem	460
3.2. δ -Doped Layers in GaAs	461
3.3. Electron Bound State on the Helium Surface	461
3.4. Band Structure of a Lateral-Surface Superlattice	462
3.5. Band Structure of a T-Wire Superlattice	463
3.6. The Aharonov-Bohm Effect in Two-Dimensional Systems	463
3.7. Impurity States in T-Shaped Quantum Wire	465
3.8. Impurity States and Image-Charge Effect in a Semiconductor Heterojunction	465
3.9. Two-Particle States: Exciton Resonance in Biased Double Quantum Dot	466
3.10. Two-Particle States: The Excitonic Aharonov-Bohm Effect Revisited	466
3.11. Three-Particle States: Trions in Double Quantum Dots	467
3.12. Real Time Evolution: Exciton Dynamics in an Double Dot Molecule	468
3.13. Real Time Evolution: Rings with Two or Three Leads	469

3.14. Spatial-Dependent Spin Precession in Double Quantum Dots	469
4. The Semiconductor Bloch Equation and the Exciton Absorption Spectra	470
4.1. Magnetoexcitons in T-Wires Under Applied Electric Field	471
4.2. Nonlinear Optical Absorption	472
5. Conclusions	473
Acknowledgment	473
References	473

1. INTRODUCTION

Free charged carriers confined in low-dimensional semiconductor structures of nanometric sizes have their motions fully quantized. Therefore, the knowledge of the energy levels and the corresponding quantum states of the confined carriers are determinant to the comprehension of the fundamental properties, both electronic and optical, of these structures. Hence, there have been developed and employed several numerical methods,^{1–10} within different approximations, in order to find the quantum states. Among the most common approximations is the use of effective masses accounting for the fast periodicity of the crystal lattice potential. This approximation has proven reasonably good despite the finite number of atoms in the lattice of the host material interacting with the confined carriers. Within the effective-mass approximation, the determination of the quantum states resides in the calculation of the slow-varying part of the wave functions,

*Author to whom correspondence should be addressed.

known as the envelope wave functions, which are given by multiband versions of the Schrödinger equation as a result of the $k \cdot p$ perturbation approach used to simplify the band structure. The solutions of these equations for spatially confined states require boundary conditions related to the sizes of the systems. Therefore, the treatment of these equations in real space representation is better suited than the use of momentum space representations which are usually applied when dealing with spatially extended states.

Many semiconductor structures presently grown have sizes large enough to accommodate many-folds of quantum states. This requires the knowledge not only of the ground state but also of the excited states in order to describe several properties of the system. Besides, the Coulomb interaction between carriers has to be taken into account if more than one carrier, in the same or in different bands, is in the system. Another important issue to be addressed in the numerical simulations is the presence of external fields since electric and magnetic fields, both static or time dependent, are commonly used to probe the quantum states.

In this review we present a numerical method to solve the Schrödinger equation, within the effective-mass approximation, for semiconductor systems. The method is particularly interesting in the solution of spatially confined states since it uses real-space coordinates, although it can also be easily modified to deal with linear momentum coordinates appropriated for periodic boundary conditions. The method allows the calculation of excited quantum states, the inclusion of interaction between carriers and the treatment of external fields.

The numerical method described here derives from the finite difference in real space applied to propagate the wave functions in infinitesimal time steps. The time-evolution operator is written in a unitary form by separating the actions of the kinetic and potential operators (procedure known as “split-operator” method). The time propagation scheme can be done also with the time taken as an imaginary number, then the method leads an initial-guessed wave function to the ground state of the system. We have extended this procedure to calculate also the excited states as well as many-particle states. All this is done without any approximations other than the ones implicit in the derivation of the starting version of the Schrödinger differential equation and the finite differencing of the derivatives for numerical implementations of such equation.

The remainder of this article goes as follows. Section 2 gives a detailed description of the method aiming to make it comprehensive and easy-to-use even for beginners in this field. Section 3 is devoted to the presentation and discussions of the application of the numerical method to solve several semiconductor systems. The optical absorption spectra calculated from an extension of the method to solve the Semiconductor Bloch Equations are discussed in Section 4. Section 5 is the conclusion and final remarks.

2. FORMULATION OF THE METHOD

This section is devoted to the presentation of the general formulation of the numerical method as well as to the discussion of some variants of the general formulation.



Marcos H. Degani earned a B.S. in physics from The Federal University of São Carlos (UFSCar), Brazil in 1982. He completed his M.Sc. in 1983 working with the properties of electrons on liquid helium, and his Ph.D. in physics 1988, where he has studied theoretically the electron-phonon interaction in low dimensional systems at University of São Paulo (USP), Brazil under the supervision of Professor Oscar Hipólito. He was a postdoc at the Material Science Division of the Argonne National Laboratory, Illinois, USA where he has worked with Molecular Dynamics applied to superconductors from 1988 to 1990. He also was a Visitor Research at the Beckman Institute for Advanced Science and Technology, University of Illinois, at Urbana, USA., in 1991. His research interests are in the optical properties, electronic structure and transport of semiconductors nanostructures.



Marcelo Zoega Maialle graduated (1986) and received master's degree (1989) in Physics from Universidade de São Paulo – São Carlos. Ph.D. in Physics from University of California – San Diego (1994), under orientation of Professor Lu J. Sham working on spin-dependent optical properties of semiconductor structures. Present interests are still related to spin-dependent phenomena and other electronic and optical properties of semiconductor nanostructures.

2.1. Real-Time Evolution of the Wave Function: General Formulation

The formal expression for advancing the wave function $\Psi(\mathbf{r}, t)$ by one infinitesimal time increment Δt is given by

$$\Psi(\mathbf{r}, t + \Delta t) = e^{-iH\Delta t/\hbar} \Psi(\mathbf{r}, t) \quad (1)$$

where the Hamiltonian is

$$H = T + V(\mathbf{r}) \quad (2)$$

with the kinetic energy operator $T = \mathbf{P}^2/2m^*$ being given in the space representation as $T = -\hbar^2\nabla^2/2m^*$ and V being the potential energy operator. m^* is the effective mass within the one band model.

Unfortunately the operation in Eq. (1) can not be done exactly, therefore approximations are needed to evolve the wave function. Several approximations can be made, for instance by breaking the exponential operator as products of other exponentials (procedure known as “split-operator” method), for example,

$$\begin{aligned} e^{-iH\Delta t/\hbar} &= e^{-i(T+V)\Delta t/\hbar} \\ &= e^{-iV\Delta t/\hbar} e^{-i\mathbf{P}^2\Delta t/2\hbar m^*} + O(\Delta t^2) \end{aligned} \quad (3)$$

$$\begin{aligned} e^{-i(T+V)\Delta t/\hbar} &= e^{-iV\Delta t/2\hbar} e^{-i\mathbf{P}^2\Delta t/2\hbar m^*} e^{-iV\Delta t/2\hbar} \\ &\quad + O(\Delta t^3) \end{aligned} \quad (4)$$

$$\begin{aligned} e^{-i(T+V)\Delta t/\hbar} &= e^{-iaV\Delta t/2\hbar} e^{-ia\mathbf{P}^2\Delta t/2\hbar m^*} e^{-iV\Delta t/2\hbar} \\ &\quad \times e^{-ia\mathbf{P}^2\Delta t/2\hbar m^*} e^{-iaV\Delta t/2\hbar} \\ &\quad + O(\Delta t^4) \end{aligned} \quad (5)$$

with $a = (3 + i\sqrt{3})/6$. The error introduced in those expressions when dropping the terms $O(\Delta t^n)$ results from the non-commutability of the kinetic and potential operators. For instance, Eq. (4) is obtained from the fact that $e^{A+B+A} = e^A e^B e^A$ only when the commutation relations $[A, [A, B]] = [B, [A, B]] = 0$ are satisfied. The evolutions Eqs. (3)–(5) are made of unitary operators therefore they preserve the norm of the wave function and thus guarantees the conservation of probability and the unconditional stability of the method.

Technically, in order to perform the numerical calculations the wave function and the potential are written for discrete positions on a grid which can be uniform or not (usually the non-uniform mesh introduces bigger errors). The symmetry of the system to be studied is another important aspect from the technical viewpoint since different methods can be used to apply the kinetic operator to the wave function. If the system has spacial periodicity it is possible to use the Fast Fourier Transform (FFT) which is fast and precise. However, the presence of external fields breaks this symmetry and something different has to be done for calculating the derivatives, for example, in finite differences the solution can be reduced to the

inversion of a matrix. We will show below in details all these approximations.

Let us choose the approximation described in Eq. (4) to exemplify an 1D propagation. It is straightforward to generalize and implement this method to two and three dimensions as it is discussed below (Sec. 2.4). For the 1D case,

$$\Psi(x, \Delta t) \simeq e^{-iV\Delta t/2\hbar} e^{-ip^2\Delta t/2\hbar m^*} e^{-iV\Delta t/2\hbar} \Psi(x, 0) \quad (6)$$

The wave function and the potential are represented on a grid and the first step of the propagation procedure is to multiply in each grid point the initial wave function $\Psi(x, 0)$ by $e^{-iV\Delta t/2\hbar}$, generating the function $\xi(x) = e^{-iV\Delta t/2\hbar} \Psi(x, 0)$. The next step is the calculation of the kinetic term. Here, for periodic systems the FFT can be used since this operator is diagonal in the momentum space. In this case, the Fourier transform ξ_k of the function $\xi(x)$ is calculated, and then multiplied by $e^{-ik^2\Delta t/2\hbar m^*}$, that is,

$$\begin{aligned} \eta(x) &= e^{-ip^2\Delta t/2\hbar m^*} \xi(x) \\ \text{IP : } 150.140.174.93 \quad \text{Tue, 13 Apr 2010 10:07:45} \quad &= \sum_{n=0}^{\infty} \frac{(i\hbar/2m^*)(d^2/dx^2))^n}{n!} \sum_k \xi_k e^{ikx} \\ &= \sum_k \xi_k e^{-ik^2\Delta t/2\hbar m^*} e^{ikx} \end{aligned} \quad (7)$$

The inverse FFT of this product is then calculated to return the function $\eta(x)$ in the direct space. Next, $\eta(x)$ is multiplied for each grid point by $e^{-iV\Delta t/2\hbar}$ to give us the wave function $\Psi(x, \Delta t)$. This scheme of propagation is repeated and the time evolution of the wave function is obtained.

When external fields are present in the system, periodic boundary condition should not be applied. Then the following approximation for the kinetic term can be used. Take $\kappa = -ip^2/2\hbar m^*$, then

$$\begin{aligned} e^{-ip^2\Delta t/2\hbar m^*} &= e^{\kappa\Delta t} \\ &= 1 + \kappa\Delta t + \frac{(\kappa\Delta t)^2}{2!} + \frac{(\kappa\Delta t)^3}{3!} + \dots \\ &= 1 + \frac{\kappa\Delta t}{2} + \frac{\kappa\Delta t}{2} + \frac{(\kappa\Delta t)^2}{4} + \frac{(\kappa\Delta t)^2}{4} + O(\Delta t^3) \\ &= \left(1 + \frac{\kappa\Delta t}{2} + \frac{(\kappa\Delta t)^2}{4} + O(\Delta t^3)\right) \cdot \left(1 + \frac{\kappa\Delta t}{2}\right) \\ &\simeq \left(1 - \frac{\kappa\Delta t}{2}\right)^{-1} \cdot \left(1 + \frac{\kappa\Delta t}{2}\right) \end{aligned} \quad (8)$$

that is,

$$e^{-ip^2\Delta t/2\hbar m^*} \simeq (1 + ip^2\Delta t/4\hbar m^*)^{-1} (1 - ip^2\Delta t/4\hbar m^*) \quad (9)$$

This approximation keeps the operator unitary and the error introduced is of the same order as in Eq. (4), i.e., $O(\Delta t^3)$. Then

$$\eta = (1 + ip^2\Delta t/4\hbar m^*)^{-1} (1 - ip^2\Delta t/4\hbar m^*) \xi \quad (10)$$

and applying the inverse operation

$$(1 + ip^2 \Delta t / 4\hbar m^*) \eta = (1 - ip^2 \Delta t / 4\hbar m^*) \xi \quad (11)$$

Using for the numerical derivatives: $f_j'' = (f_{j-1} - 2f_j + f_{j+1})/\delta^2$ and $f_j' = (f_{j+1} - f_{j-1})/2\delta$ with δ being the distance between the points of the (uniform) grid, the expression above can be written as

$$(1 - ip^2 \Delta t / 4\hbar m^*) \xi \Rightarrow \xi_j + \beta(\xi_{j-1} - 2\xi_j + \xi_{j+1}) \quad (12)$$

$$(1 + ip^2 \Delta t / 4\hbar m^*) \eta \Rightarrow \eta_j - \beta(\eta_{j-1} - 2\eta_j + \eta_{j+1}) \quad (13)$$

with $\beta = i\hbar \Delta t / 4m^* \delta^2$, then Eq. (11) reads

$$\begin{aligned} -\beta\eta_{j-1} + \eta_j(1 + 2\beta) - \beta\eta_{j+1} \\ = \beta\xi_{j-1} + \xi_j(1 - 2\beta) + \beta\xi_{j+1} \end{aligned} \quad (14)$$

This has the form of a tridiagonal matrix, and since the right hand side of this equation is known, the inversion of this matrix yields the function $\eta(x)$. This approximation can be used with different boundary conditions, periodic or not. Let us see how.

2.1.1. Boundary Condition for Finite Systems

At the edge of the system the wave function must vanish, that is, $\eta_0 = \eta_{N+1} = 0$. Then Eq. (14) becomes

$$\begin{aligned} & \begin{pmatrix} 1+2\beta & -\beta & 0 & 0 \\ -\beta & 1+2\beta & -\beta & 0 \\ 0 & -\beta & 1+2\beta & -\beta \\ 0 & 0 & -\beta & 1+2\beta \end{pmatrix} \begin{pmatrix} \eta_1 \\ \vdots \\ \eta_N \end{pmatrix} \\ &= \begin{pmatrix} 1-2\beta & \beta & 0 & 0 \\ \beta & 1-2\beta & \beta & 0 \\ 0 & \beta & 1-2\beta & \beta \\ 0 & 0 & \beta & 1-2\beta \end{pmatrix} \begin{pmatrix} \xi_1 \\ \vdots \\ \xi_N \end{pmatrix} \end{aligned} \quad (15)$$

2.1.2. Boundary Conditions for Periodic Systems

In this case $\eta_0 = \eta_1 = \eta_N = \eta_{N+1}$. Then Eq. (14) becomes

$$\begin{aligned} & \begin{pmatrix} 1+\beta & -\beta & 0 & 0 \\ -\beta & 1+2\beta & -\beta & 0 \\ 0 & -\beta & 1+2\beta & -\beta \\ 0 & 0 & -\beta & 1+\beta \end{pmatrix} \begin{pmatrix} \eta_1 \\ \vdots \\ \eta_N \end{pmatrix} \\ &= \begin{pmatrix} 1-\beta & \beta & 0 & 0 \\ \beta & 1-2\beta & \beta & 0 \\ 0 & \beta & 1-2\beta & \beta \\ 0 & 0 & \beta & 1-\beta \end{pmatrix} \begin{pmatrix} \xi_1 \\ \vdots \\ \xi_N \end{pmatrix} \end{aligned} \quad (16)$$

Note that only the first and the last elements of the diagonal are changed when comparing Eq. (16) with Eq. (15).

After obtaining η from the inversion of either Eq. (15) or (16), the wave function $\Psi(x, \Delta t)$ is calculated at each grid point by multiplying $e^{-iV\Delta t/2\hbar}$. Performing this procedure repeatedly, Δt after Δt , an initial wave function $\Psi(x, 0)$ can be evolved to the final state $\Psi(x, t)$. This is the backbone of the numerical method.

2.2. Imaginary-Time Propagation: Energy Spectrum

In order to obtain the energy spectrum and the corresponding wave functions for a given potential, the same scheme of propagation described above can be used. The spectral method we use was derived from the work of Feit et al.¹ The time-dependent Schrödinger equation with a real time t is transformed into a diffusion equation by replacing t by $-i\tau$. Now the normalization of the wave function must be done during the propagation (due to an exponential decrease), and after several time steps the system converges to the ground state of the system. The advantage of this scheme, when comparing to the original method of Feit et al.¹ is that we obtain the wave function and the energy value simultaneously which allows us to use this method in self-consistent calculations. Besides, excited states are obtained using the Gram-Schmidt algorithm. Let us see how all this is done.

First it is shown how the imaginary-time evolution leads to the ground state. Consider a time-independent Hamiltonian H with eigenstates and eigenvalues given by $|\phi_n\rangle$ and ε_n , respectively, such that $\varepsilon_0 < \varepsilon_1 < \varepsilon_2 < \dots < \varepsilon_n$. Any given state $|\Psi(t)\rangle$ can be written as

$$|\Psi(t)\rangle = \sum_n a_n \exp\left(-i\frac{\varepsilon_n t}{\hbar}\right) |\phi_n\rangle \quad (17)$$

Taking $t = -i\tau$,

$$|\Psi(\tau)\rangle = \sum_n a_n \exp\left(-\frac{\varepsilon_n \tau}{\hbar}\right) |\phi_n\rangle \quad (18)$$

which can be normalized and written as

$$|\Psi(\tau)\rangle^{\text{norm}} = \frac{\sum_n a_n \exp(-\varepsilon_n \tau / \hbar) |\phi_n\rangle}{\sqrt{\sum_n |a_n|^2 \exp(-2\varepsilon_n \tau / \hbar)}} \quad (19)$$

Note that the normalization depends on τ , therefore it must be calculated at each time step of the propagation.

Equation (19) can be rewritten as

$$|\Psi(\tau)\rangle^{\text{norm}} = \frac{|\phi_0\rangle + \sum_{i>0} \frac{a_i}{a_0} \exp((\varepsilon_0 - \varepsilon_i)\tau / \hbar) |\phi_i\rangle}{\sqrt{1 + \sum_{i>0} |\frac{a_i}{a_0}|^2 \exp((\varepsilon_0 - \varepsilon_i)\tau / \hbar)}} \quad (20)$$

from which it can be seen that

$$\lim_{\tau \rightarrow \infty} |\Psi(\tau)\rangle^{\text{norm}} = |\phi_0\rangle \quad (21)$$

showing that the imaginary-time evolution leads to the ground state.

Let us now obtain the excited states. An given excited state can be written as

$$|\varphi_1\rangle = \sum_n b_n e^{-\varepsilon_n \tau / \hbar} |\phi_n\rangle \quad (22)$$

and it is assumed that the ground state $|\Psi_0\rangle = |\phi_0\rangle$ is already known.

The Gram-Schmidt method of orthonormalization is used to obtain the new excited eigenstate Ψ_1

$$|\Psi_1(\tau)\rangle = \frac{|\varphi_1(\tau)\rangle - \langle\Psi_0(\tau)|\varphi_1(\tau)\rangle|\Psi_0(\tau)\rangle}{\sqrt{\langle\varphi_1(\tau)|\varphi_1(\tau)\rangle - |\langle\Psi_0(\tau)|\varphi_1(\tau)\rangle|^2}} \quad (23)$$

where

$$\langle\varphi_1|\varphi_1\rangle = \sum_n |b_n|^2 e^{-2\varepsilon_n \tau / \hbar} \quad (24)$$

$$\langle\Psi_0|\varphi_1\rangle = \langle\phi_0|\varphi_1\rangle = b_0 e^{-\varepsilon_0 \tau / \hbar} \quad (25)$$

Then, Eq. (23) can be written as

$$|\Psi_1(\tau)\rangle = \frac{|\phi_1\rangle + \sum_{i>1} \frac{b_i}{b_1} \exp((\varepsilon_1 - \varepsilon_i)\tau/\hbar) |\phi_i\rangle}{\sqrt{1 + \sum_{i>1} |\frac{b_i}{b_1}|^2 \exp(2(\varepsilon_1 - \varepsilon_i)\tau/\hbar)}} \quad (26)$$

and since $\varepsilon_0 < \varepsilon_1 < \dots < \varepsilon_n$,

$$\lim_{\tau \rightarrow \infty} |\Psi_1(\tau)\rangle = |\phi_1\rangle \quad (27)$$

that is, the first excited eigenstate is found. The procedure can be repeated to obtain the other eingesates including the ones which are energy degenerated.

In practice, for all states being calculated, the excited states are obtained using the Gram-Schmidt algorithm to keep the orthogonalization among the states

$$|\Psi_n\rangle_{\text{new}} = |\Psi_n\rangle - \sum_{j=1}^{n-1} \langle\Psi_j|\Psi_n\rangle |\Psi_j\rangle \quad (28)$$

A set of guessed initial states are defined and simultaneously propagated in (imaginary) time. At each time step all the wave functions are calculated and “forced” by the Gram-Schmidt method to be orthogonal to other states. The wave functions in this process must be normalized, and after several time steps, the set of states converge to the set of eigenstates of the system.

Some interesting aspects of this method are:

- (1) Good stability;
- (2) Fast convergency;
- (3) Very little dependence on the initially guessed state;
- (4) It can be applied to a wide range of potentials;
- (5) It gives simultaneously the eigenvalues and eigenstates;
- (6) The same basic procedure can be applied to real- as well as imaginary-time propagations.

2.3. Band Structure of Periodic Systems

For a periodic system (assuming here an 1D system) the Bloch's condition tell us that $\Psi(x) = e^{iQx}\phi(x)$, with $\phi(x)$ periodic and Q within the Brillouin zone. In this case the propagation is made as following

$$\begin{aligned} \Psi(x, \Delta t) &\simeq e^{-iV\Delta t/2\hbar} e^{-ip^2\Delta t/2\hbar m^*} e^{-iV\Delta t/2\hbar} \Psi(x, 0) \\ &= e^{-iV\Delta t/2\hbar} e^{-ip^2\Delta t/2\hbar m^*} e^{-iV\Delta t/2\hbar} \\ &\quad \times e^{iQx} \phi(x) \end{aligned} \quad (29)$$

Using the FFT, the kinetic term is

$$\begin{aligned} \eta(x) &= e^{-ip^2\Delta t/2\hbar m^*} e^{iQx} \xi(x, 0) \\ &= \sum_k \xi_k e^{-i(Q+k)^2 \Delta t / 2\hbar m^*} e^{ikx} \end{aligned} \quad (30)$$

For each value of Q the states are calculated [as above, Eq. (7)] and the bands are generated as functions of Q . Different bands are given when excited states are calculated (see previous section).

2.4.1 Higher Spatial Dimensions and Many Particles

The method described above for an 1D system can be easily implemented to higher dimensions. The difference now is that the momentum \mathbf{P} and the position \mathbf{r} operators have components along the additional directions. However, operators related to directions which are orthogonal commute making trivial to extend the method to these other directions. To exemplify this let us consider again the action of the momentum (vector) operator

$$\eta(\mathbf{r}, t + \Delta t) = \exp \left[-\frac{i\mathbf{P}^2 \Delta t}{2m^* \hbar} \right] \xi(\mathbf{r}, t + \Delta t) \quad (31)$$

In order to perform this operation the momentum is written in terms of its components $\mathbf{P}^2 = P_x^2 + P_y^2 + P_z^2$. Since these components commute with each other, the action of the exponential operator with the kinetic energy can be simplified (exactly) as

$$\begin{aligned} \eta(\mathbf{r}, t + \Delta t) &= \exp \left[-\frac{iP_x^2 \Delta t}{2m^* \hbar} \right] \exp \left[-\frac{iP_y^2 \Delta t}{2m^* \hbar} \right] \\ &\quad \times \exp \left[-\frac{iP_z^2 \Delta t}{2m^* \hbar} \right] \xi(\mathbf{r}, t + \Delta t) \end{aligned} \quad (32)$$

The approximation already given in Eqs. (8) and (9) remains valid and therefore Eq. (11) for higher dimensions reads

$$(1 + i\mathbf{P}^2 \Delta t / 4\hbar m^*) \eta(\mathbf{r}) = (1 - i\mathbf{P}^2 \Delta t / 4\hbar m^*) \xi(\mathbf{r}) \quad (33)$$

The remaining procedure are similar to the 1D case already discussed.

Systems with many particles can also be studied by this method. For example, the wave function for an electron in a 2D system can be expressed as $\Psi(x, y, t)$; the

eigenstates of this problem can be obtained following the method described above. Fortunately, exactly the same formalism can be used to describe two particles in 1D, interacting or not, where x represent the coordinate of one particle and y the coordinate of the other one. This is the case, for example, of an exciton (electron–hole pair) in 1D systems. In the special case of identical particles, if the Hamiltonian does not mix spin and spatial coordinates, the total wave function is a product of a spatial function and the spin function (not included explicitly in the formalism). The spatial function is calculated by the method described here, and by choosing the appropriated symmetry of the function it is possible identify the singlet and triplet states. For the singlet state, the spin function must be anti-symmetric for the exchange of two particles, therefore the spatial function must be symmetry. The triplet states, on the contrary, are the anti-symmetry spatial functions for the two-particle exchange. In principle, it is possible to calculate the wave function of N interacting particles $\Psi(x_1, y_1, z_1, \dots, x_N, y_N, z_N, t)$ without using the approximation of products of single particle wave functions. Then it is avoided the discussion of direct and exchange Hartree terms since the wave functions are of many particles from the start.

2.5. Self-Consistent Potentials

Here the inclusion of a potential depending on the electronic density is treated via a self-consistent method. It is considered as an illustration for the general procedure a particular case of a quasi-1D system (quantum wire) in which the electrons are free along the wire whereas perpendicularly to the wire the bound electronic state are solved including self consistency. The 3D wave function is then written as

$$\Psi_{n,k_z}(\vec{r}) = \frac{\exp(ik_z z)}{\sqrt{L_z}} \phi_n(x, y) \quad (34)$$

where k_z is the wavevector in the z direction (wire axis) with L_z being the wire length. The energy is given by

$$E_{n,k_z} = \varepsilon_n + \frac{\hbar^2 k_z^2}{2m^*} \quad (35)$$

The bound states in the plane perpendicular to the wire are $\phi_n(x, y)$ with eigen-energies ε_n . They are given by the Schrödinger equation in 2D

$$\left[-\frac{\hbar^2}{2m^*} \left(\frac{\partial^2}{\partial x^2} + \frac{\partial^2}{\partial y^2} \right) + V_{ef}(x, y) \right] \phi_n(x, y) = \varepsilon_n \phi_n(x, y) \quad (36)$$

with the total potential $V_{ef}(x, y)$ being the sum of $V_{ext}(x, y)$ (due to the wire structure) with the Hartree potential describing the electron–electron interactions, i.e.,

$$V_{ef}(x, y) = V_{ext}(x, y) + V_H(x, y) \quad (37)$$

V_H is given by the Poisson equation

$$\nabla^2 V_H(x, y) = \frac{4\pi e^2}{\epsilon} \rho(x, y) \quad (38)$$

$$\rho(x, y) = -n(x, y) + N_d(x, y) - N_a(x, y) \quad (39)$$

where ϵ is the dielectric constant, $n(x, y)$ is the electron density

$$n(x, y) = \sum_i N_i |\phi_i(x, y)|^2 \quad (40)$$

N_d and N_a are the ionized donor and residual acceptor densities, respectively. N_i is the total electronic density in the i -th subband, which is determined from

$$N_i = \begin{cases} \frac{L_z}{\pi a_0} \cdot \sqrt{\frac{k_B T 2m^* a_0^2}{\hbar^2}} F_{-1/2}(\eta_i) & \text{if } T \neq 0 \\ \frac{2L_z}{\pi a_0} \cdot \sqrt{\frac{2m^* a_0^2}{\hbar^2}} \cdot \sqrt{\varepsilon_F - \varepsilon_i} & \text{if } T = 0 \end{cases} \quad (41)$$

where a_0 is the effective Bohr radius, ε_i the i -th subband energy, T is the temperature ε_F the Fermi energy. $F_{-1/2}(\eta_i)$ is the Fermi-Dirac distribution function and $\eta_i = (\varepsilon_F - \varepsilon_i)/k_B T$.

For periodic boundary conditions, where the states are characterized by wave vectors, the solutions involving the Poisson equation Eq. (38) are simplified. As an illustration, a system periodic only along the x direction is considered. Then using Fourier transform

$$v_H(x, y) = \mathcal{F}[v(k_x, y)] = \frac{1}{2\pi} \sum_{k_x} e^{-ik_x x} v(k_x, y) \quad (42)$$

$$\rho^*(x, y) = \mathcal{F}[\rho(k_x, y)] = \frac{1}{2\pi} \sum_{k_x} e^{-ik_x x} \rho^*(k_x, y) \quad (43)$$

where it was defined dimensionless quantities $v_H = V_H/Ry$ and $\rho^* = \rho a_0^3/\epsilon$, with $Ry = (e^2/2a_0)$ being the effective Rydberg energy. With these changes Eq. (38) reads

$$-k_x^2 v(k_x, y) + \frac{\partial^2 v(k_x, y)}{\partial y^2} = 8\pi \rho^*(k_x, y) \quad (44)$$

Using finite difference in a uniform grid of points, spaced by δ , in the y direction,

$$\frac{2v_{j-1}}{2\delta^2} - \left(\frac{2}{\delta^2} + k_x^2 \right) v_j + \frac{2v_{j+1}}{2\delta^2} = 8\pi \rho_j^* \quad (45)$$

where for each value of k_x it is defined $v(k_x, y) \Rightarrow v_j$ and $\rho^*(k_x, y) \Rightarrow \rho_j^*$. Or equivalently

$$av_{j-1} + bv_j + cv_{j+1} = 4\pi \rho_j^* \quad (46)$$

with

$$a = \frac{1}{2\delta^2} \quad (47)$$

$$b = -\left(\frac{2}{\delta^2} + \frac{k_x^2}{2} \right) \quad (48)$$

$$c = \frac{1}{2\delta^2} \quad (49)$$

In order to go further and solve the Poisson equation the boundary conditions have to be defined. The edge of the system in the y direction is given by the points $j = 0$ and $j = N_y + 1$ in the grid. For these points the potentials are set as v_0 and v_{N_y+1} . Therefore for the neighboring points $j = 1$ and $j = N_y$, the Hartree potential are determined from

$$-\left(\frac{2}{\delta^2} + k_x^2\right)v_1 + \frac{2v_2}{2\delta^2} = 8\pi\rho_1^* - \frac{2v_0}{2\delta^2} \quad (50)$$

$$-\left(\frac{2}{\delta^2} + k_x^2\right)v_{N_y} + \frac{2v_{N_y-1}}{2\delta^2} = 8\pi\rho_{N_y}^* - \frac{2v_{N_y+1}}{2\delta^2} \quad (51)$$

Defining

$$\tilde{\rho}_0 = \frac{1}{8\pi} \frac{v_0}{\delta^2} \quad (52)$$

$$\tilde{\rho}_{N_y} = \frac{1}{8\pi} \frac{v_{N_y+1}}{\delta^2} \quad (53)$$

the Poisson equation can be written in the form of a tridiagonal matrix

$$\begin{pmatrix} b & c & 0 & 0 & 0 & \cdots & 0 \\ a & b & c & 0 & 0 & \cdots & 0 \\ 0 & a & b & c & 0 & \cdots & 0 \\ 0 & 0 & a & b & c & \cdots & 0 \\ 0 & 0 & 0 & a & b & \cdots & \vdots \\ \vdots & \vdots & \vdots & \vdots & \vdots & \ddots & c \\ 0 & 0 & 0 & 0 & 0 & a & b \end{pmatrix} \cdot \begin{pmatrix} v_1 \\ v_2 \\ v_3 \\ v_4 \\ v_5 \\ \vdots \\ v_{N_y} \end{pmatrix} = 8\pi \begin{pmatrix} \rho_1 \\ \rho_2 \\ \rho_3 \\ \rho_4 \\ \rho_5 \\ \vdots \\ \rho_{N_y} - \tilde{\rho}_{N_y} \end{pmatrix} \quad (54)$$

The solution for the potential $v_j = v_j(k_x)$ is obtained by the inversion of this matrix. Finally $v(x, y)$ is calculated by the inverse Fourier transform

$$v_H(x, y) = \mathcal{F}[v(k_x, y)] = \frac{1}{2\pi} \sum_{k_x} e^{-ik_x x} v(k_x, y) \quad (55)$$

This potential is used in the Schrödinger equation Eq. (36). To start the simulation the Hartree potential is made zero and the Schrödinger equation is used to calculate the initial wave functions. Then the Poisson's equation is solved with the electronic density which depends on the calculated wave functions. Again the Schrödinger equation is solved including the new Hartree potential, and new wave functions are calculated, and this process continues until a convergence on the energy levels is achieved.

3. APPLICATIONS OF THE METHOD TO LOW-DIMENSIONAL SEMICONDUCTOR STRUCTURES

In this section several applications of the method are described and discussed. It is not intended to discuss the

physics behind each example treated, for that the reader is directed to the original works in the references. Instead, emphasis is given to the particular aspects of each system investigated which motivated characteristic modifications in the basic formulation of the method.

3.1. The Stark Ladder Problem

Here it is given the first example of the application of the method. The system considered contains electronic states created in a set of 15 coupled quantum wells, namely a GaAs-AlAs superlattice, under applied electric field.¹¹ In the directions perpendicular to the system growth axis the states are taken as plane waves due to the translational invariance. Therefore it suffices to calculate the 1D states created by the set of quantum wells. For that, the system potential comprehends an active region containing the wells and separating barriers as well as two barrier regions on both edges of the system. The electric field F gives an additional contribution to the potential as $V(z) = -eFz$. The ground state is obtained through the propagation of an initially guessed electron wave packet (e.g., a Gaussian wave function) in imaginary time and the excited states are obtained by the orthonormalization procedure described in the basic formalism of Section 2.2. Figure 1 shows the energy levels calculated for the 30 quantum

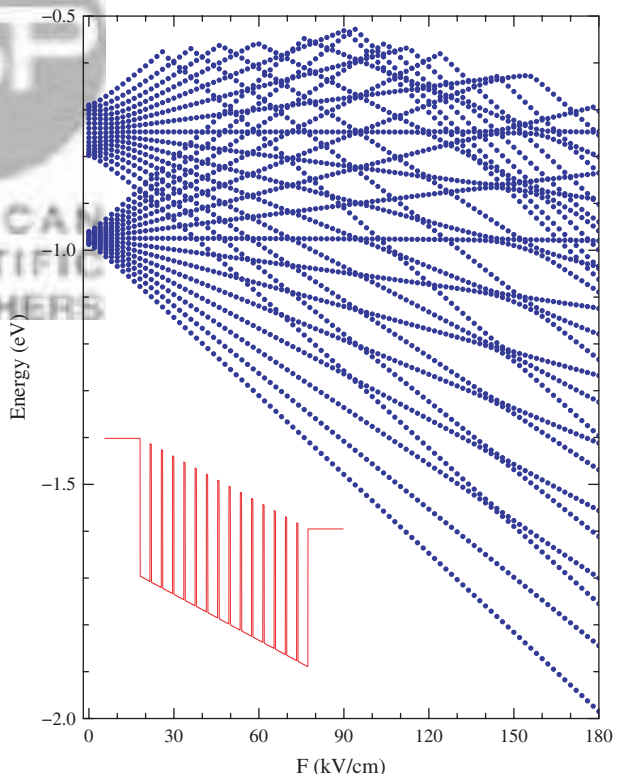


Fig. 1. Energy levels as functions of the applied electric field for the electronic states in a GaAs-AlAs superlattice with 15 coupled quantum wells. Two minibands are seen which under the electric field opens into ladders of states. Unpublished.

states of lowest energies as functions of the applied electric field. It is observed that for zero electric field there are two distinct groups of 15 states, each group corresponding to a miniband of delocalized states with bandwidth of 27 meV and 107 meV. As the field increases, the states in each miniband opens into a ladder of states differing in energy by eFd (where d is the period of the superlattice). This effect is known as the Wannier-Stark localization in a superlattice of which the first experimental evidence was reported by Mendez et al.¹² and by Voisin et al.¹³ It is interesting to note that for large field values, $F > 30$ kV/cm, the energy levels associated with higher-energy minibands appear in the spectrum demonstrating that the method of calculating excited states is robust in finding states which may derive of symmetries different than those initially guessed.

In summary, this simple example illustrates the treatment of one electron in a finite-size system, with 1D potential including an applied electric field, and the calculation of many excited states.

3.2. δ -Doped Layers in GaAs

In this application of the method the electronic states of a single δ -doped layer in GaAs are investigated. Here the δ -doped layer is a thin planar region of single atomic layer in bulk GaAs which is uniformly doped.¹⁴ The problem is still essentially 1D since the states along the plane of the δ -doped layer are assumed as plane waves in view of the translational invariance. Again the system was treated with a finite size and the eigenstates, including the excited ones, were calculated. The novelty here is the inclusion of the interaction between the electrons, which is done by an one-body Schrödinger equation including self-consistency with the Hartree and exchange-correlation potentials [see Section 2.5]. These potentials are functions of the spatial-dependent electron density which in turn are determined by the wave functions being calculated, leading to the self consistency. In Figure 2 the effective potential and the energy levels are shown for two temperatures (which ultimately affects the number of electrons per unit area) including two possible dopant diffusion profiles in the doping layer (a uniform and a Gaussian dopant distributions).

A variant of the δ -doping problem was treated considering a system with multiple Si δ -doped layers in GaAs forming a superlattice potential along the growth direction.¹⁵ The essence of this problem is the same of the single δ -doped layer just discussed, that is, self-consistent potential is used. However, now the system is no longer finite since it consists of an infinitely long superlattice. For that it is used periodic boundary conditions [see Eqs. (7) and (16) in Section 2.1] treating only a single period of the superlattice. Due to the infinitely long system the quantum states are labeled by a continuous index k_z which is the wave vector along the growth direction. This index is

Delivered by Internet
University of
IP : 150.140.1
Tue, 13 Apr 2010

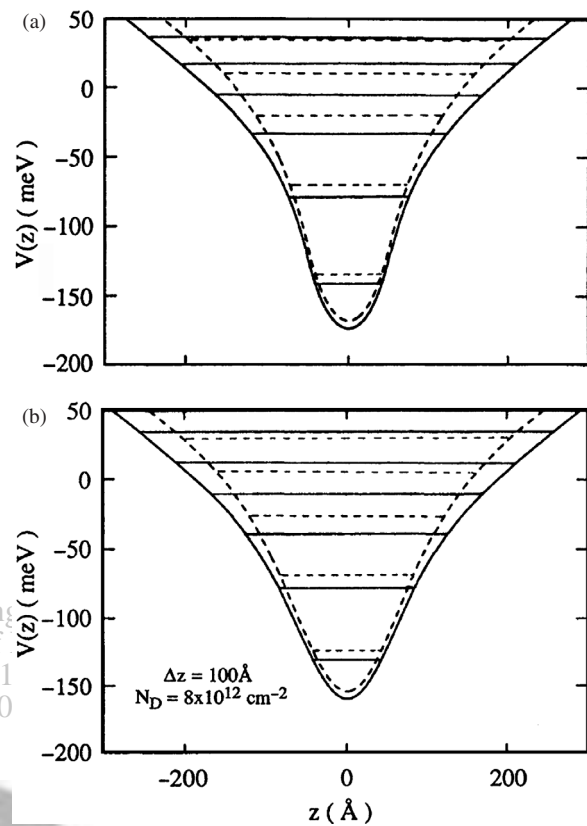


Fig. 2. Effective potential and energy levels for a δ -doped layer in bulk GaAs for $T = 0$ K (solid curves) and $T = 300$ K (dashed curves). The dopant in the layer are assumed in a (a) uniform distribution and in a (b) Gaussian distribution. All energies are relative to the Fermi energy. Reprinted with permission from [14], M. H. Degani, *Phys. Rev. B* 44, 5580 (1991). © 1991, American Physical Society.

just a parameter in the Schrödinger equation which can be varied to construct the subband structure of the superlattice. Another modification to the basic formalism of the numerical method applied in this problem is the derivatives in the z coordinate, present in the kinetic operator, which were done essentially exact in the momentum space, since this operator is diagonal in the reciprocal space. After performing these derivatives in the reciprocal space the wave functions were transformed back to the real space by fast Fourier transform (see Section 2.1).

3.3. Electron Bound State on the Helium Surface

In this example the quantum states of an electron in the vacuum bound to the helium surface by the Coulomb interaction with its classical image charge is numerically investigated.¹⁶ Along the helium surface the electron states are plane waves, so the problem is once again an 1D case of the Schrödinger equation for the direction perpendicular to the surface. The potential includes the contributions from the image charge effect, the application of an electric field perpendicular to the surface and also a magnetic field applied parallel to the surface. The three lowest energy

states were calculated as functions of the fields to obtain the energy transitions between the states, which were successfully compared with recent experimental data.¹⁷ Figure 3 shows (a) the effective bounding potential and (b) the transition energies compared to the experiments. It was important to include a potential modification given by the diffuseness of the liquid–vapor helium interface in order to achieve a good agreement with the experiment.

In this work¹⁶ it was also investigated the lifetime of an electron bound to the helium surface when the electric field is applied in the opposite direction, that is, the field is pulling the electron away from the surface. For this study an initial electron wave packet calculated by the imaginary-time procedure and the it was evolved in real time (see Section 2.1). The inverse lifetime Γ as a function of the electric field is plotted in Figures 3(c and d). It is shown a series of snap shots of the fundamental wave function being pulled away from the helium surface by the applied field. More applications using real time propagation are found in Sections 3.12–4.

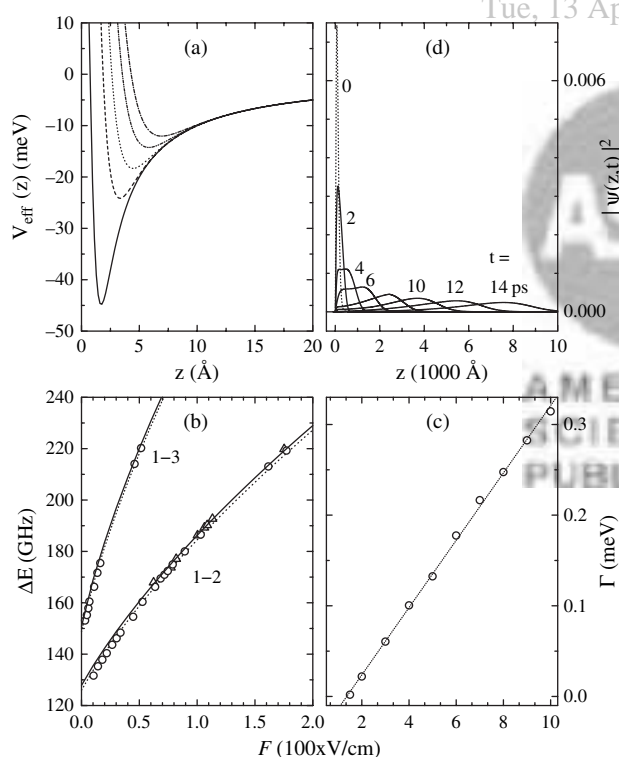


Fig. 3. (a) Effective potential for temperatures. $T = 0$ K (solid), 0.5 K (dashed), 1.0 K (dotted), 1.5 K (dashed-dotted-dotted), and 2.0 K (dashed-dotted). (b) Transition energy between ground state and first (1-2) and second excited states (1-3), as a function of an external electric field applied perpendicular to the helium surface, for two values of the helium liquid temperature, $T = 1.0$ K (solid line) and $T = 1.3$ K (dotted line). Symbols are the experimental data.¹⁷ (c) Lifetime to unbind the electron from the surface with an applied electric field F ($T = 1.0$ K). (d) Time evolution of the ground state wave function when $F = 500$ V/cm and $T = 1.0$ K. Reprinted with permission from [16], M. H. Degani et al., *Phys. Rev. B* 72, 125408 (2005). © 2005, American Physical Society.

3.4. Band Structure of a Lateral-Surface Superlattice

The solving method is now applied to obtain the band structure of electronic states on a 2D superlattice, namely, a planar periodic potential which can be realized in practice by gates created from nanolithography techniques nearby a 2D electron gas. The novelty of this application¹⁸ is to extend our formulation to obtain 2D states. Due to the periodicity on both directions of the planar superlattice, the states satisfy the Bloch's theorem and a 2D wave vector is used to characterizes the quantum states together with a band index. As in the case of the δ -doped superlattice discussed above, the periodicity of the potential favors the action of the kinetic operator on the wave fuctions in the momentum space. Fast Fourier transform is then used to return to the real space. The solving method is applied to each wave vector of a mesh chosen within the Brillouin zone and the excited states, obtained by the orthogonalization procedure, correspond to the different bands of the band structure.

In Figure 4 it is shown the band structure for wave vectors along the [01] and [11] reciprocal lattice directions. From this band structure it is possible to observe that the method calculate equally well the localized states (being represented by the flat bands for the lowest energy states) as well as the extended states having a large bandwidth.

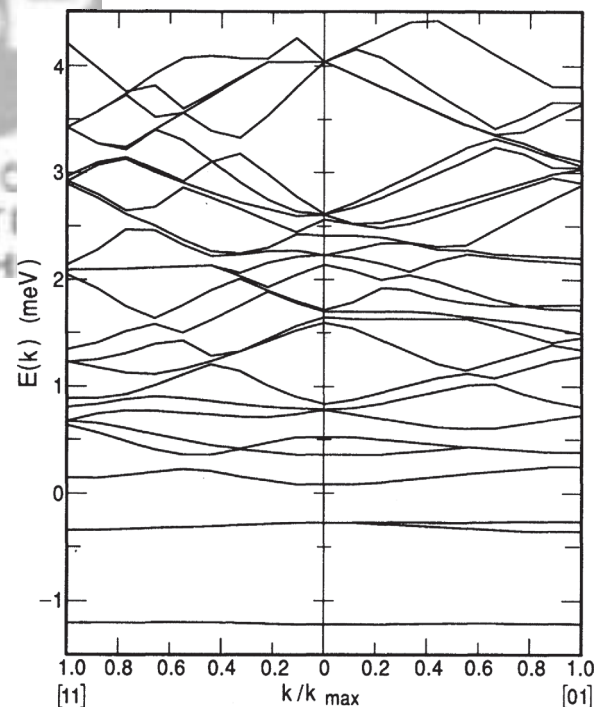


Fig. 4. Dispersion relation (energy versus wave vector) along the directions [01] and [11] for the lateral superlattice. The 25 lowest subbands are calculated. Reprinted with permision from [18], M. H. Degani and J. P. Leburton, *Phys. Rev. B* 44, 10901 (1991). © 1991, American Physical Society.

3.5. Band Structure of a T-Wire Superlattice

The system investigated can be realized by using the so-called cleaved edge overgrowth technique. Its fabrication consists of three main steps: first, a superlattice of GaAs/AlGaAs (stem wells) is grown on a (001) substrate, then after cleavage, a GaAs quantum well (arm well) is grown over the exposed (110) surface, resulting in a T-shaped active region. A gate can be used to control the electronic population in this arm well and electronic transport along it can also be studied. A gate produce an electric field perpendicular to the arm well and control the depletion layer. The size Y (see Fig. 5) mimics the electric field effect, and as it can be seen in the dispersion relation it changes significantly the electronic behavior. For $Y = 0$ the system is a simple quantum well. For increasing Y it is observed an increasing band gap and, interestingly, the excited subband changes inclination predicting negative effective masses for $Y = 11$ nm.

3.6. The Aharonov-Bohm Effect in Two-Dimensional Systems

This section addresses the Aharonov-Bohm effect (ABE), i.e., an angular momentum change caused by an applied magnetic field, in electronic states in 2D structures.

Firstly, the ABE in electron states in a 2D quantum ring is discussed.¹⁹ For that, the magnetic field is applied

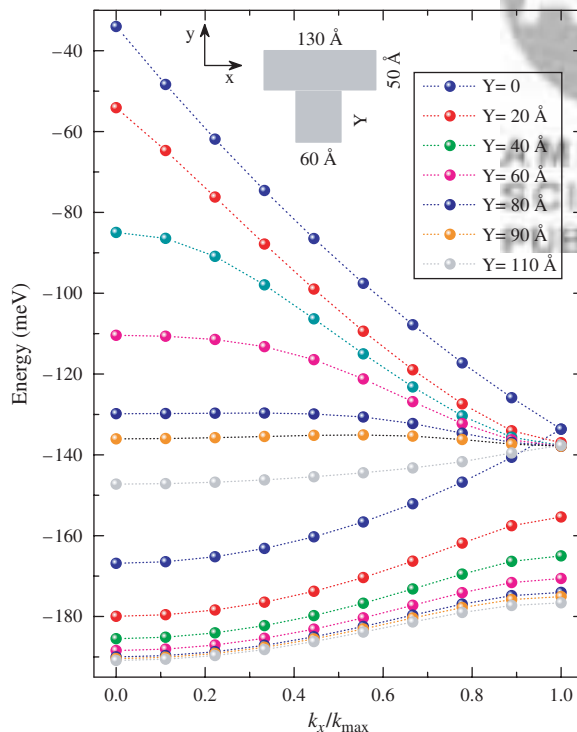


Fig. 5. Dispersion relation for a superlattice of T-wires shown for different values of the size Y , which mimics the effect of an electric field along the y direction. Unpublished.

perpendicularly to the plane of the ring which confines the electron in an circular section (ringlike) region with an inner and outer radii. The systems investigated are either perfectly circular rings or elliptical shaped rings. The numerical method treats both geometries in the same way, that is, both are described by a large square region with a rectangular mesh points over which the potentials are defined. The method, in this case, solves 2D wave functions and the corresponding energies for a small number of lowest energy states as functions of the applied magnetic field. In Figure 6 we see how the energy spectra of these states behave with the intensity of the magnetic field in a perfectly circular quantum ring. It is observed that, as the field increases, there are energy level crossings and the ground state can change its angular momentum component. This is a signature of the ABE.

In Figure 7 the lowest energy states are shown for the circular and for elliptical quantum rings. In the latter case it is seen that the crossings of energy levels no longer occur. Now, the anticrossings result from angular momentum mixing due to the potential with reduced symmetry.

Still motivated by the ABE in 2D systems, we have investigated²⁰ the possibility of observing this effect in excitonic states by optical measurements. A type-II planar structure was considered in which the electron stayed in a quantum dot with the hole attracted to it by the Coulomb

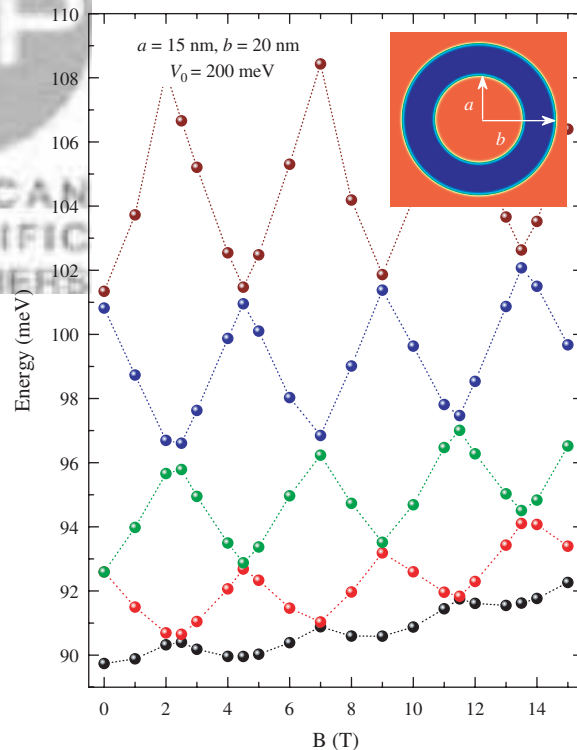


Fig. 6. Energy levels for an electron in a quantum ring as functions of the applied magnetic field. At $B = 0$ the levels are two-fold degenerated and labeled according to the angular momentum l along the magnetic field. For $B \neq 0$ the states split $l = \pm m$, with $m = 0, 1, \dots$. Unpublished.

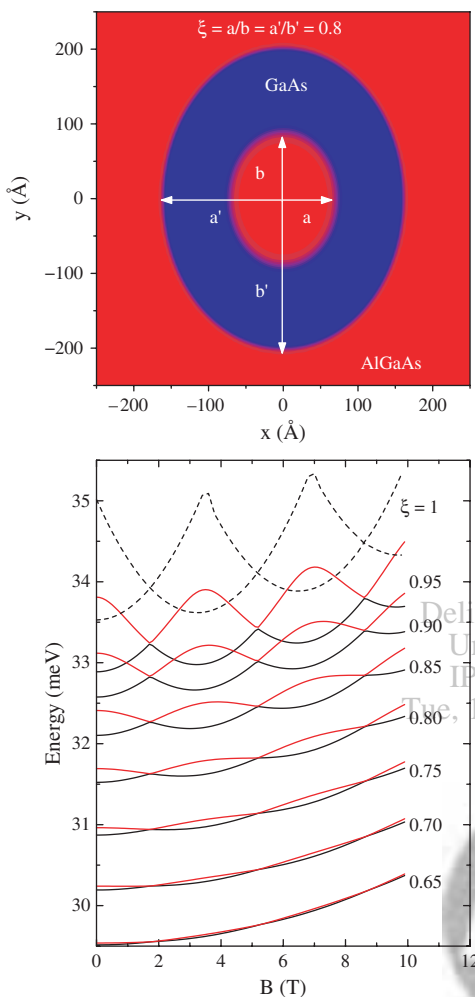


Fig. 7. Energies of the two lowest energy states versus the magnetic field. Results are shown for different elliptical rings as shown by the parameter ξ . Reprinted with permission from [19], G. A. Farias et al., *Phys. Rev. B* 77, 085316 (2008). © 2008, American Physical Society.

interaction but at the same time forced to stay around of the quantum dot by the type-II potential profile. Since the hole is only weakly bound to the confined electron, the hole energy levels are very close to each other, which demanded the calculation of a large number of excited states. On the other hand, in view of the strong confinement of the electron in the dot, the problem was simplified by separating the two-particle (electron-hole) wave function into a product of wave functions for the electron and hole. The electron state was considered independent of the Coulomb attraction due to the strong dot confinement and the hole states are bound to the electron in the dot by the Coulomb attraction. The treatment of the electron-hole wave function without separation was also done and it is discussed below in Section 3.10.

In Figure 8 it is shown the exciton energies as functions of the applied magnetic field. The ABE aspect of the exciton energy spectra is similar to the one for the electron ABE described earlier in Figure 6. Now, however,

the spectra were plotted with the data point sizes weighted by the optical oscillator strength (basically the electron-hole spatial overlap). These figures can be seen as the optical absorption spectra related to the exciton photoexcitation. It was observed that the exciton ABE, seen from the optical absorption spectra, can be hidden by the loss of optical oscillator strength of the ground state when its angular momentum changes with increasing magnetic field. This results from the fact that the strongest oscillator strengths are those for electron and hole wave functions with similar symmetries, and since the electron has circular symmetric (angular momentum component $L_e = 0$) the hole states with $L_h \neq 0$ are weakly coupled to the light. Figure 8 exemplifies the changes in the spectra for: (a) a circular quantum dot, (b) a circular quantum dot with rough interface, (c) a dot with a nearby negative impurity, and (d) an elliptical dot. In all cases the reduction in symmetry mixes the angular momentum components of the exciton states. The numerical program used to treat

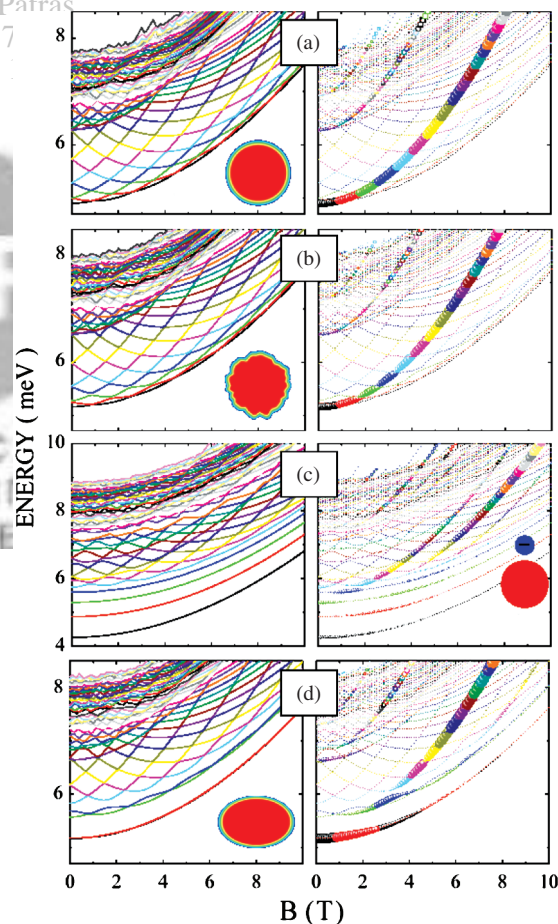


Fig. 8. Energy levels for excitons in type-II quantum dots as functions of the applied magnetic field. (a) circular dot; (b) roughness of the dot walls; (c) dot with a nearby impurity and (d) elliptically shaped dot. The sizes of the data points on the right-hand side panels are proportional to the optical oscillator strength. Reprinted with permission from [20], M. H. Degani et al., *Phys. Rev. B* 78, 075322 (2008). © 2008, American Physical Society.

all the cases is exactly the same, only the potential profile of the dot was changed. This is possible because the numerical method does not rely in basis set expansion and it is, consequently, easily applied to systems with different symmetries. Also, this example shows the necessity of some problems in knowing a large number of excited states to properly describe the system. Our numerical approach could handle this nicely and up to 60 excited states were calculated.

3.7. Impurity States in T-Shaped Quantum Wire

The numerical method has been used to calculate electronic states in a 3D structure with the wave function depending explicitly on all the three coordinates (x, y, z). The system presently investigated²¹ is the same as in Section 3.5, that is the T-quantum-wire structure (see Fig. 5).

The T-wire can have its ground state calculated by separating the direction along the wire and directions perpendicular to it. That is, essentially a 2D problem could be solved to find the fundamental state because along the wire the wave functions are plane waves due to the translational symmetry. However, we have investigated the states in the presence of a hydrogenic donor impurity which makes the problem truly 3D. The interesting aspect of this system is that the attractive impurity potential competes with the bound state created in the stem-arm intersection, and this competition is strongly dependent on the relative position of the impurity and the intersection region.

The numerical method is applied using periodic boundary conditions for the directions on the plane of the arm well (xy plane) and a finite size for the z direction perpendicular to this plane. A large enough supercell was used to assure each cell was independent from the neighboring ones.

In Figure 9(a) it is shown the electron fundamental energies for two different T-wires: structure A has the stem well of width 7 nm and structure B 8 nm, both with the arm well 7 nm wide. The impurity is kept at $x_i = y_i = 0$ and the energies are presented as functions of the impurity coordinate z_i ($z = 0$ nm is in the middle of the arm well, the stem well is located at $z < 0$). It is observed that for the structure A the electron fundamental state stays preferably around the T-wire than around the impurity when the latter was brought along the stem well (negative increase of z_i). This can be seen in Figure 9(b) for the average z projection of the electron wave functions. On other hand, structure B, having a wider stem well, can have the electron bound to the impurity even when the latter is in the stem well. The projections of the electron wave functions on the xz are also shown for three different situations exemplifying what was just said.

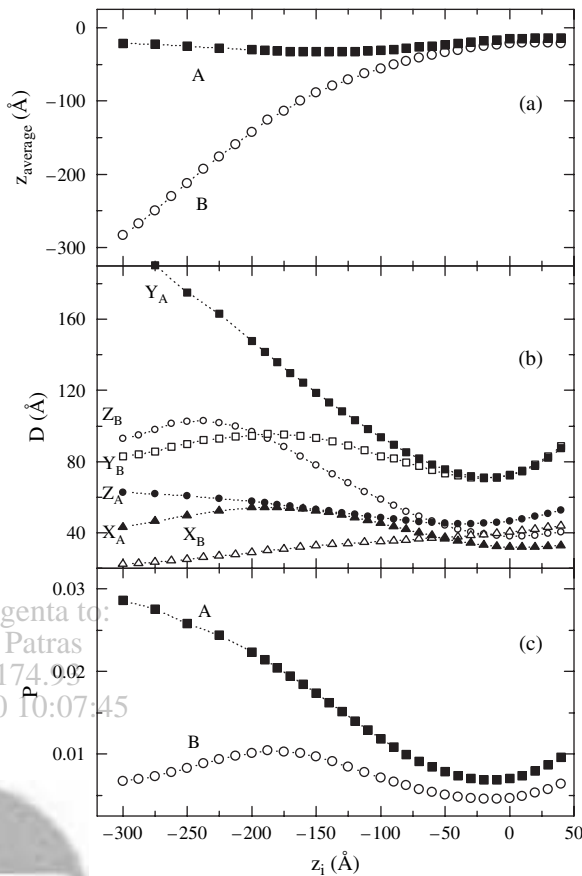


Fig. 9. Full symbols are for sample A (7 nm \times 7 nm) and open symbols are for sample B (7 nm \times 7 nm). (a) Average position along the z axis as a function of the impurity position. (b) Standard deviation as a function of the impurity position z_i . (c) Participation ratio P as a function of the impurity position; smaller P mean stronger 3D localization. Reprinted with permission from [21], M. H. Degani, *Phys. Rev. B* 66, 233306 (2002). © 2002, American Physical Society.

3.8. Impurity States and Image-Charge Effect in a Semiconductor Heterojunction

A physically similar problem to the one discussed in the previous section was investigated by Belita et al.²² considering the competition between the binding potentials of an impurity and a metal-oxide-semiconductor (MOS) interface showing image charge effects, such as in metal-SiO₂-Si interfaces. In this case, the image charge potential attracts the electron to the interface and such potential competes with the attractive potential of an impurity located near the interface. An electric, and also a magnetic field, can be used to control the competition between these attractive potentials. What this effectively creates is a system of two interacting quantum dots with energy levels controlled by the external fields. We have improved the solutions of Ref. [22] by treating this problem without any approximations. Using a finite system with the appropriated boundary conditions, the 3D electronic wave functions were solved exactly, and an investigation was

done as function of the fields (electric and/or magnetic) which were varied to created resonances between the quantum states localized around the impurity and nearby the interface. In Figure 10 the effective potential seen by the electron near the MOS interface is shown for two values of electric field. The ground state and the first excited state are also shown. As the electric field changes these states exchange positions between the surface and the near-impurity. This is better seen in Figure 11 where the energies and the average positions of these two states are shown as functions of the applied electric field.

3.9. Two-Particle States: Exciton Resonance in Biased Double Quantum Dot

The method is now applied to study quantum states of two interacting particles. The problem of an exciton (i.e., an interacting electron–hole pair) is investigated here for a square wire with a double dot embedded on it. In this way, the motions of the electron and hole in the transverse directions to the wire can be assumed frozen and the motions along the wire are investigated. The system Hamiltonian includes the kinetic energy of both particles, the band offset potentials along the wire axis, the effect of an electric field along this axis and the Coulomb attraction between the electron and hole. This interaction is treated as an average over the transverse fundamental states for the electron and hole, i.e.

$$V_{eh}(z) = \frac{e^2}{4\pi\epsilon} \int \frac{dx_e dy_e dx_h dy_h |\phi_0^e|^2 |\phi_0^h|^2}{\sqrt{z^2 + (x_e - x_h)^2 + (y_e - y_h)^2}} \quad (56)$$

where $\vec{\rho}_\alpha = (x_\alpha, y_\alpha)$ and $\phi_\alpha(\vec{\rho}_\alpha)$, with $\alpha = e, h$, are the ground states for the transverse direction.

The system investigated²³ is a double quantum dot with two dots of different widths along the wire axis. In this way the fundamental wave function, at zero electric field,

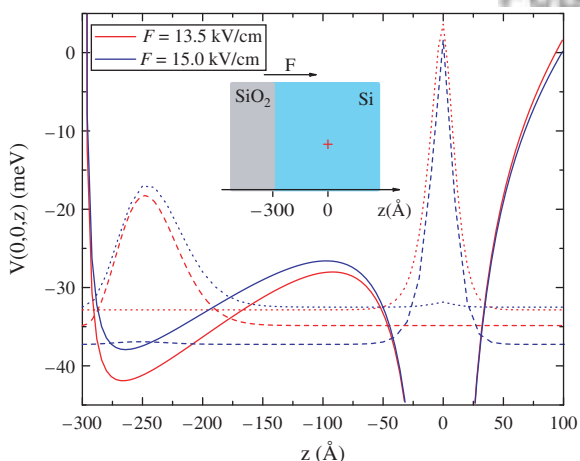


Fig. 10. Projection of the effective potential and projection of the wave functions of the two lowest energy states for two values of applied electric field F . The inset shows the schematics of the system with the impurity located at $z = 0$. Unpublished.

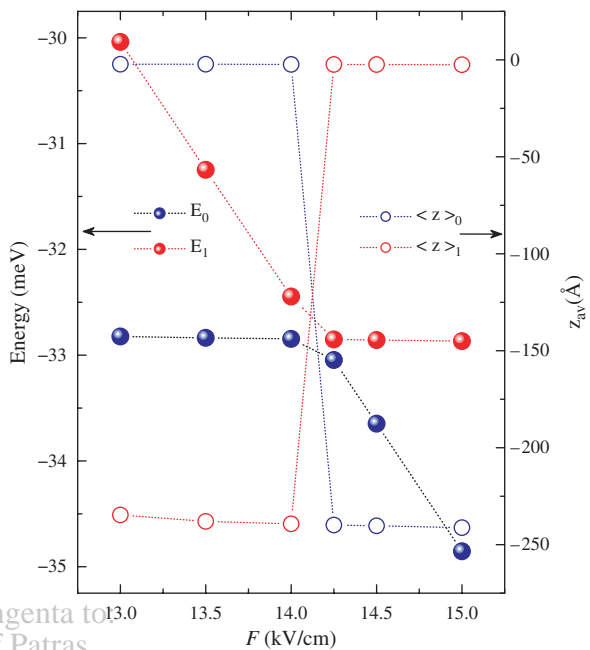


Fig. 11. Energies and average electronic positions as functions of the applied electric field for the two lowest energy states. Unpublished.

consists of an electron and a hole localized in the wider dot and the first excited state has the particles extending mostly over the narrower dot. The electric field is used to control this spatial distribution of carriers. When different energy levels become resonant the electron (or hole) wave functions of the resonant levels can be found on both dots. In this process the Coulomb attraction between the electron and hole is important and was the object of investigation. Figure 12 shows the exciton energy of the four lowest energy states as functions of the applied electric field. Negative field tends to bring the fundamental and excited electron states into resonant whereas positive fields acts in the same way for the hole states. When the energy spectra of the four states are plotted with the data points scaled by optical oscillator strength (basically the electron and hole wave function overlaps), Figure 13 represents the optical absorption spectra showing the interplay between the exciton states governed by the Coulomb interaction between the pair of particles in the exciton.

3.10. Two-Particle States: The Excitonic Aharonov-Bohm Effect Revisited

When discussing the Aharonov-Bohm effect in Section 3.6 it was argued that a simplification of the problem was done in separating the exciton wave function as a product of the electron and hole wave functions. In order to check the validity of such approximation the exciton state was also solved for two interacting particles.²⁰ In this case, the treatment of the two particles is for a 2D system and, since the problem is numerically more demanding, only the three lowest energy states were calculated as functions of the

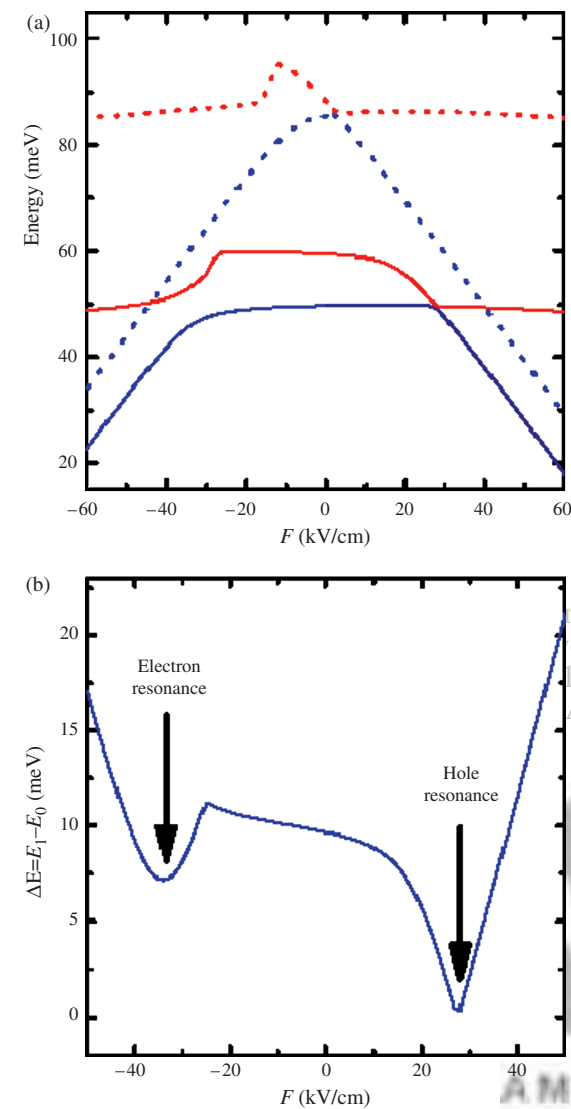


Fig. 12. (a) Energy spectrum versus applied electric field; only the two lowest energy states shown; dotted lines: no Coulomb interaction; full lines: exciton. (b) Differences between the lowest excitonic energies. Resonances are seen at fields of $\simeq -35$ kV/cm and $\simeq 27.5$ kV/cm [values of the energy in (a) taken from the first lateral (x, y) subband]. Reprinted with permission from [23], M. H. Degani et al., *Appl. Phys. Lett.* 89, 152109 (2006). © 2006, American Institute of Physics.

applied magnetic field. A good agreement between the exact case discussed here and the approximative approach of separable wave functions is a consequence of the particular type-II quantum dots investigated which strongly confine the electron in the dots. In Figure 14 the energies of the fundamental and two excited states are shown in comparison with the results of the approximative approach already presented in Figure 8.

3.11. Three-Particle States: Trions in Double Quantum Dots

Recently, trions, i.e., bound complexes of two electrons and one hole (X^-) or two holes and one electron (X^+), in

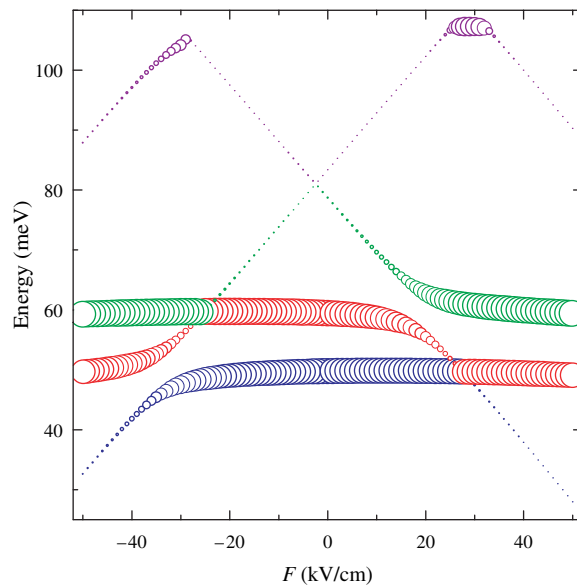


Fig. 13. Spectrum showing the four lowest eigen-energies; circles' sizes vary in proportion to the overlap of the electron and hole wave functions. Reprinted with permission from [23], M. H. Degani et al., *Appl. Phys. Lett.* 89, 152109 (2006). © 2006, American Institute of Physics.

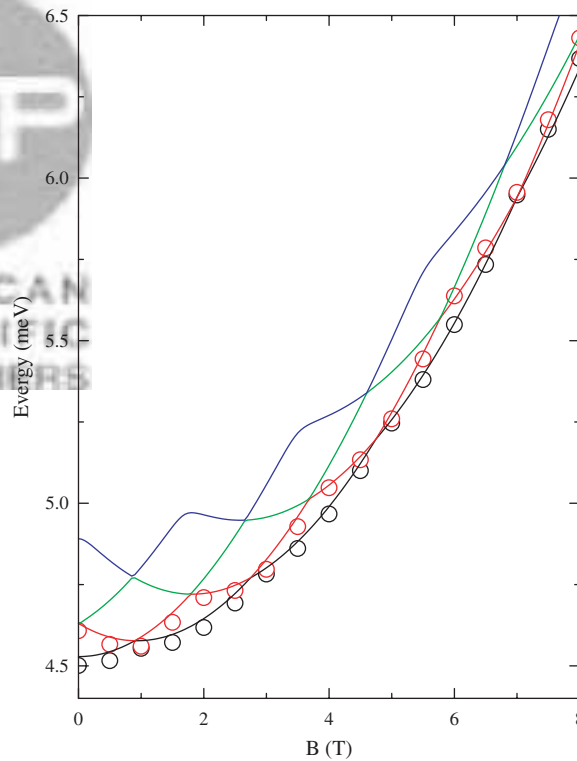


Fig. 14. Energies of an exciton in a type-II circular quantum dot as functions of the applied magnetic field. Symbols are for the calculation with wave function of two-interacting particles. Lines are for the simplified calculation using separable wave functions for the electron and hole, as in Figure 8. Reprinted with permission from [20], M. H. Degani, et al., *Phys. Rev. B* 78, 075322 (2008). © 2008, American Physical Society.

semiconductor quantum dots were experimentally investigated with a precision never before achieved.²⁵ An applied electric field was used to control the carriers' localization in an asymmetric double dot and energy level crossings as well as singlet-triplet spin mixing could be investigated in details.

In order to simulate the trion states in double dot systems, a simplified model for the dots was constructed considering the carriers confined to a 1D wire containing an asymmetric double dot.²⁴ The problem was separated along the wire axis and for the directions transverse to the wire. For the transverse directions the states were solved and then considered unaffected by the carriers' motions along the wire, just as before in Section 3.9. Then the numerical method was used to obtain the states of the three particles along the wire axis in the effective potential of the double dot, with the applied electric field in this direction, and Coulomb interactions between the carriers as in Eq. (56). In this 1D case the wave functions have three coordinates, $\psi(x_1, x_2, x_3)$, one for each particle, and up to four lowest energy states were calculated. Recalling that the trion has two particles which are similar (two holes for X^+ or two electrons for X^-) and one particle of a different type (one electron or one hole, respectively), the final trion state must be anti-symmetric over the exchange of the two similar particles' coordinates as well as spins. The calculated wave functions did not include the spin states and symmetric and anti-symmetric wave functions over the exchange of similar particles' spatial coordinates followed naturally from the numerical method. Due to the requirement of the overall anti-symmetry, the spatial-coordinate-symmetric states are then associated to the singlet-spin states whereas the coordinate-anti-symmetric states are associated to the spin-triplet states.

The transition energies between the trion states and the one-carrier (final) states were calculated in order to confront with the measured photoluminescence signal. In Figure 15(a) are shown the trion X^+ and the hole final states and the associated transition energies Figure 15(b) as functions of the applied electric field (for the range of fields favoring the two hole states to be resonant and extended over the two dots). In Figure 16 the transitions energies are plotted with the size of the data points weighted by the trion-hole optical oscillator strength. This "X" shaped spectra were observed experimentally,²⁵ and our numerical model has the merit of describing it without using any fitting parameter.

The inclusion of a spatial-dependent spin interaction was also investigated²⁶ since spin mixing between the singlet and triplet states were measured.²⁷ Again, the numerical simulation of the trion could give very accurate spectra without the use of fitting parameters for the carrier spatial distribution. In this calculation it was investigated the effects of two spatial-dependent spin mixing mechanisms: (i) the electron-hole exchange interaction and (ii) interactions with the crystal lattice spins. Both mechanisms were

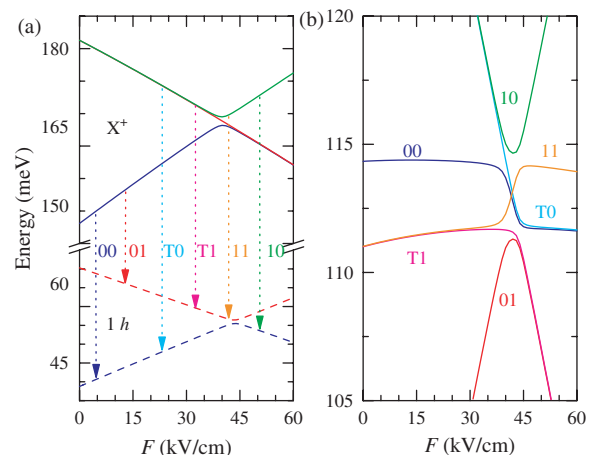


Fig. 15. Electric-field dependence of the energy levels for a X^+ trion and a hole in a system of thicknesses (left quantum dot/barrier/right quantum dot sizes) 4/4/2.5 nm. (a) Energy levels for the trion and for one hole. (b) Transition energies as indicated in (a). Reprinted with permission from [24], M. H. Degani and M. Z. Maialle, *Phys. Rev. B* 75, 115322 (2007). © 2007, American Physical Society.

modeled within a mean-field approximation and the spin mixing showed up into the optical spectra as splittings in the energy transition lines similar to the ones observed in recent experiments.²⁷

3.12. Real Time Evolution: Exciton Dynamics in an Double Dot Molecule

Returning to the study of excitons in double quantum dots, the use of an applied electric field made possible to set resonances between states localized in different dots. The resonances associated with the electron and hole states

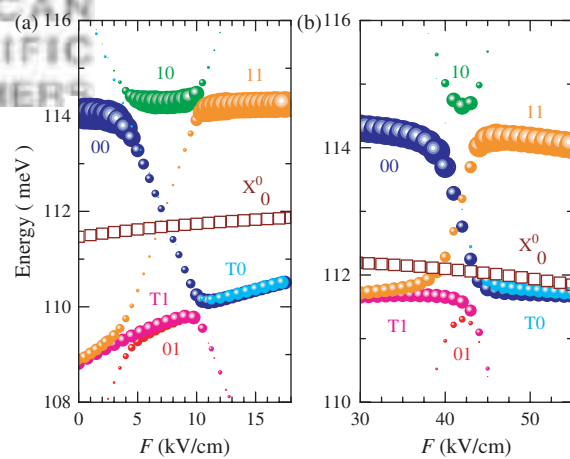


Fig. 16. Energies and oscillator strengths (the size of the symbols is proportional to the oscillator strengths) of the transitions between the X^+ trion states and the hole states in the systems: (a) 4/4/3.5 nm and (b) 4/4/2.5 nm. The exciton optical transitions X_0^0 are also shown in open-square symbols. Transitions are labeled as in Figures 15. Reprinted with permission from [24], M. H. Degani and M. Z. Maialle, *Phys. Rev. B* 75, 115322 (2007). © 2007, American Physical Society.

were set by different field values as shown in Figure 12. The resonant states exhibit charge oscillations, i.e., quantum beats, between the two dots which could be controlled by the applied electric field. This can be of interest for future applications of double dots as terahertz (THz) emitter. In Figure 17 the charge oscillations are shown for the fields causing resonances for the electron and hole states and the role of the Coulomb interaction could be assessed for comparison of the results for the exciton and for the two independent particles.

In Figure 18 the time evolution of the electron wave function is shown for the resonance at $F = -35$ kV/cm.

3.13. Real Time Evolution: Rings with Two or Three Leads

An interesting application of the real time propagation, in which the Aharonov-Bohm effect can be visualized, is the calculation of the transmission of one electron through a ring with two or three leads in the presence of a magnetic field. The system to be addressed here is a circular ring with average radius 20 nm and width 10 nm, that is $15 \text{ nm} < r < 25 \text{ nm}$ and two leads with the same width as the ring. An initial wave packet is built as a product of two functions, a Gaussian in the x direction and a sine in the y direction. This wave packet is initially ($t = 0$) localized in the lead at left of the ring and has momentum along the x direction equal to k . A magnetic field is applied perpendicular to the ring's plane and, for the parameters used ($m^* = 0.067$ and $r_{\text{avg}} = 20 \text{ nm}$), the quantum flux ϕ_0 is set at $B_0 = 3.29 \text{ T}$. It is expected maxima in the transmission

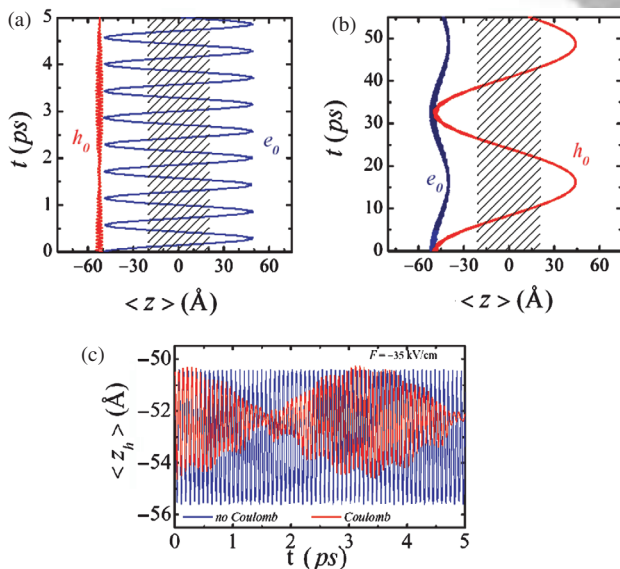


Fig. 17. Dynamical evolution of the average position for the electron (e_0) and the hole (h_0). (a) Reverse resonance ($F = -35$ kV/cm); (b) Direct resonance ($F = 27.5$ kV/cm); (c) Zooming of the regions $z_h \approx 5.3$ nm in panel (a). Reprinted with permission from [23], M. H. Degani et al., *Appl. Phys. Lett.* 89, 152109 (2006). © 2006, American Institute of Physics.

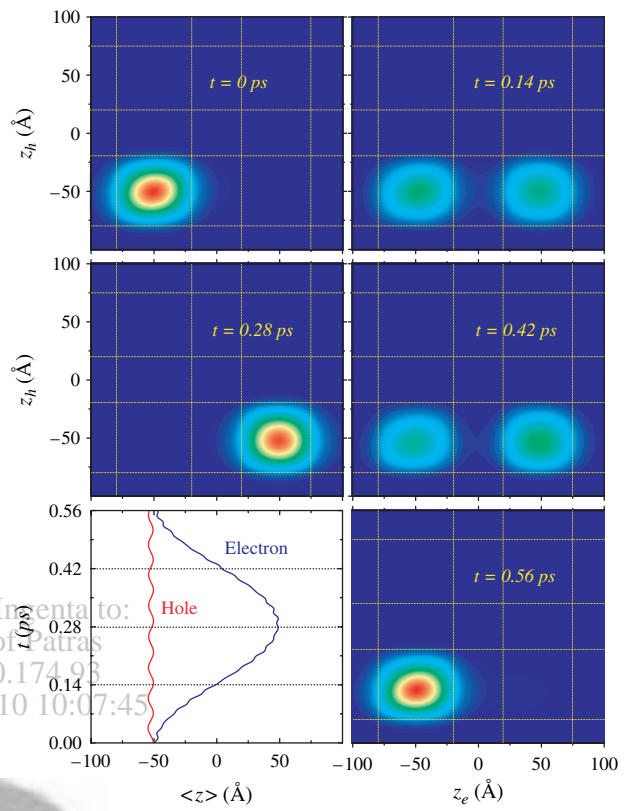


Fig. 18. Dynamical evolution of the electron wavefunction projection for the reverse resonance ($F = -35$ kV/cm). Unpublished.

through the ring for field values which are multiples of B_0 and minima for fields multiples of $B_0/2$. Figure 19 illustrates, for different values of the magnetic field, a situation where the wave packet acquires the maximum transmission through the ring for a momentum $ka_0 = 1$. Figure 20 shows the electron transmission as a function of the magnetic field for several momenta. The oscillations on the transmission show maxima and minima for multiples of B_0 and $B_0/2$, respectively.

3.14. Spatial-Dependent Spin Precession in Double Quantum Dots

Still concerned with double quantum dots in applied electric field, the spin dynamics of the electron and hole were investigated.³⁰ Now it is considered that the particles constituting the exciton could have their spin (angular momentum) dynamics affected by the effective g factors dependent on the particle position. With the application of a magnetic field perpendicular to the growth direction (Voigt geometry) the spin precessions about the field is affect by these position-dependent g factors according to the wave function distribution between the two dots, which was controlled by the electric field. Besides the electron and hole spin precessions driven by the magnetic field

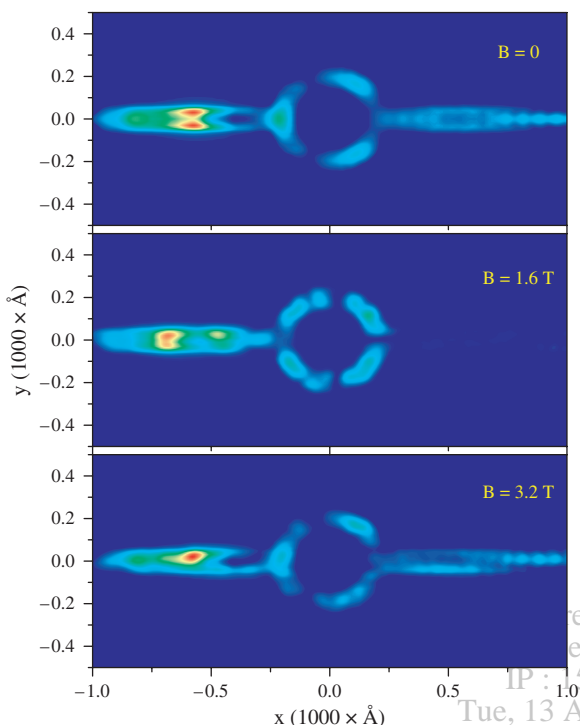


Fig. 19. Snap shots of the electronic wave function for different values of the applied magnetic field. For $B = 0$ and 3.2 T the interference in the Aharonov-Bohm effect favors the transmission, whereas for $B = 1.6$ T the contrary occurs. Unpublished.

through the g factors, the electron–hole exchange interaction coupling the electron and hole spins was included in the dynamics.

Numerically the problem was solved³⁰ by evolving in time an initial excitonic wave function (i.e., a two-particle state) in a quasi-1D system modeling the double dot. The numerical method gives the time evolution of a spinor (four spin components for the heavy-hole exciton) in a problem where position and spins could not be separated.

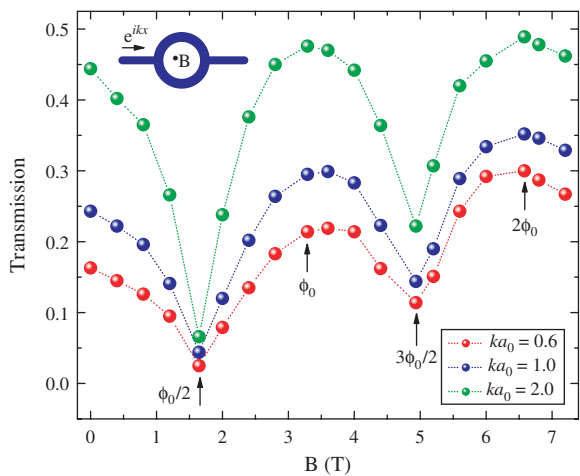


Fig. 20. Transmission through the ring as function of the magnetic field for different values of incident electron momentum. Unpublished.

From the spinor at different times the exciton spin components were calculated and by a fast-Fourier transformation the spin precession frequencies were obtained. The study could identify the different precession frequencies despite the complicated spin dynamics mediated by the electron and hole positions, an information which could be of use in future measurements.

4. THE SEMICONDUCTOR BLOCH EQUATION AND THE EXCITON ABSORPTION SPECTRA

The procedure applied to evolve in time the solutions of the Schrödinger equation was extended to treat the semiconductor Bloch equation (SBE) describing the photoexcitation process in semiconductor materials. The present approach to solve the SBE is carried out in the time domain and in the real-space domain, which are in opposition to the pioneer studies using frequency and momentum domains.

The simplest formulation of the SBE has similarity with the Schrödinger equation in the sense that the SBE is a first-order differential equation in time with the kinetic operator, in the real-space representation, being a second-order derivative in the position. Now the function under consideration is the interband optical polarization representing the creation–annihilation of electron–hole pairs. However, the SBE has also some particular characteristics such as a generation term (photocreation of excitons), dephasing terms and other terms describing the interactions between photoexcited carriers which introduces nonlinear contributions.

In what follows the SBE is used to investigate quasi-1D semiconductor systems so the interband polarization $P(z, t)$ is a function of the time t and of the electron–hole relative distance z along the 1D system axis. Within the approximation of retaining only two-point matrix densities, namely the polarization $P(z, t)$ and the carrier population $n(z, t)$, the SBE reads²⁹

$$\begin{aligned} i\hbar \frac{\partial}{\partial t} P(z, t) = & HP(z, t) + d_0 E(t)[2n(z, t) - L\delta(z)] \\ & - \frac{1}{L} \int dz' [V^{hhh}(z') + V^{eee}(z')] n(z', t) \\ & \times P(z - z', t) + \frac{2}{L} \int dz' V^{eheh}(z') \\ & \times n(z - z', t) P(z', t) \end{aligned} \quad (57)$$

$$\begin{aligned} i\hbar \frac{\partial}{\partial t} n(z, t) = & P(z, t) E^*(t) d_0^* - P^*(-z, t) E(t) d_0 \\ & - \frac{1}{L} \int dz' V^{ehhe}(z') [P(z - z', t) P^*(-z', t) \\ & - P^*(z' - z, t) P(z', t)] \end{aligned} \quad (58)$$

$$H = -\frac{\hbar^2}{2\mu} \frac{d^2}{dz^2} - V^{ehhe}(z) + \tilde{E}_g - i\hbar\Gamma \quad (59)$$

where \tilde{E}_g is an effective band gap given by the material band gap and the lateral ground-state energies of electron and hole. L is the wire (1D system) length, $z = z_e - z_h$ is the electron–hole relative coordinate along the system axis and μ is the electron–hole reduced mass. The optical pulse has an envelope $E(t)$ assumed to be a Gaussian function and Γ gives the relaxation rate within the relaxation-time approximation accounting for scattering processes causing dephasing of the optical polarization. The carrier–carrier interaction terms are calculated for the quasi-1D system using the wave functions of the fundamental states, ϕ_0^α , for the conduction and valence bands, calculated in the plane perpendicular to the wire by the average

$$V^{\alpha\alpha'\alpha'\alpha}(z) = \frac{e^2}{4\pi\epsilon} \int \frac{dx_\alpha dy_\alpha dx'_\alpha dy'_{\alpha'}}{\sqrt{z^2 + (x_\alpha - x_{\alpha'})^2 + (y_\alpha - y_{\alpha'})^2}} |\phi_0^\alpha|^2 |\phi_0^{\alpha'}|^2 \quad (60)$$

In this version of the SBE the second term on the right-hand side of Eq. (57) accounts for the phase-space filling effects which cause bleaching of the optical absorption. The third term in Eq. (57) is the exchange correlation responsible for bandgap renormalization. The last term is the so-called “local field”, that is, the local optical polarization acting as an actual electromagnetic field. These terms contribute only for intense pumping powers.

4.1. Magnetoexcitons in T-Wires Under Applied Electric Field

As a model for the quasi-1D problem it is firstly treated the quantum wire formed in the intersection of two quantum wells grown on perpendicular crystallographic directions, that is, the so-called T-shaped quantum wire already presented in Section 3.7. This choice of quasi-1D system enters in the calculation of the wave functions of the fundamental states ϕ_0^α used to obtain the Coulomb terms Eq. (57). Other choices of quasi-1D systems give qualitatively similar results. The solutions of the SBE for the direction along the wire was investigated²⁸ in the limit of low excitation power, meaning that all nonlinear terms in the SBE above discussed were vanished. For this simplest approximation only the equation of motion for the optical polarization $P(z, t)$ suffices and it reads²⁸

$$i\hbar \frac{\partial}{\partial t} P(z, t) = HP(z, t) - d_0 E(t) L \delta(z) \quad (61)$$

This equation is similar to the time-dependent Schrödinger equation with an additional term for the creation of electron–hole pairs [the last term in Eq. (61)].

The time dependent solution of the simple SBE Eq. (61) is obtained by assuming a null polarization at initial time $P(z, 0) = 0$. The real-time evolution procedure described in Section 2.1 is then applied, but now due to the presence of the source term, which is proportional to the envelope of the exciting optical field $E(t)$, there is a finite polarization for time $t > 0$. The Hamiltonian H acts on

the spatial part of the polarization and reveals the eigen-energies through the time evolution. The energy spectra of the optical absorption coefficient is then obtained from the Fourier transform of the interband polarization $P(t) = d_{cv} P(z = 0, t) + c.c.$, where d_{cv} is the conduction–valence band dipole element. Here $z = 0$ is taken for the electron–hole optical coupling in the vertical transition approximation (i.e., zero momentum transfer form the photon to the e–h pair).

Figure 21 shows in the inset the optical absorption spectra in which the lowest energy peak is due to the fundamental exciton state and the smaller peak at higher energy results from excited states close to the continuum of states (states of unbound electron–hole pairs) which appear as a flat part of the spectra. In Figure 21(a) the energy position of the fundamental exciton peak and the onset of the continuum of states are plotted as functions of the magnetic field (applied perpendicularly to the plane of the arm quantum well of the T-wire). The exciton binding

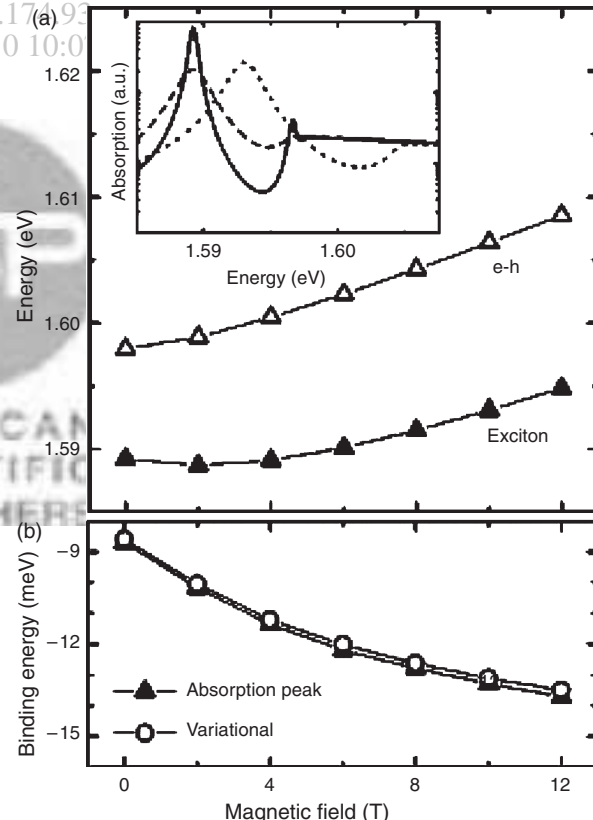


Fig. 21. (a) Electron–hole transition energy (e–h) and exciton fundamental transition energy as functions of the applied magnetic field. The inset shows the optical absorption spectra for an inverse dephasing rate $\Gamma^{-1} = 500$ fs, for $B = 0$ (dashed line) and $B = 8$ T (dotted line). The solid line is for $\Gamma^{-1} = 1000$ fs and $B = 0$. (b) Exciton energy in relation to the wire continuum as a function of the magnetic field from a variational method calculation and from the energy position of the absorption fundamental peak. Reprinted with permission from [28], J. R. Madureira et al., *Phys. Rev. B* 66, 075332 (2002). © 2002, American Physical Society.

energy, i.e. the energy difference between the two energies plotted in Figure 21(a), is plotted in Figure 21(b). Also, an approximated result from a variational method calculation is shown demonstrating the good agreement between the results from these two different approaches.

The effect of an applied electric field along the wire axis is illustrated in Figure 22. This is the essence of the Franz-Keldish effect, that is, the dissociation of the exciton by an electric field, which is visualized by the increase of the optical absorption linewidth and by the merging of the exciton peak with the continuum. The applied magnetic field yields different excitonic binding energy, but if the linewidths are plotted (Fig. 22(d)) as functions of a normalized electric field F^* , basically given by a ratio between the electric field energy across the exciton and the exciton binding energy, then all the results follow the same dependence on F^* . This clearly shows the competition between the electric field and the excitonic binding energy for different magnetic field values.

4.2. Nonlinear Optical Absorption

The SBE including nonlinear contributions were also treated for T-wire systems, now with the stem well tilted

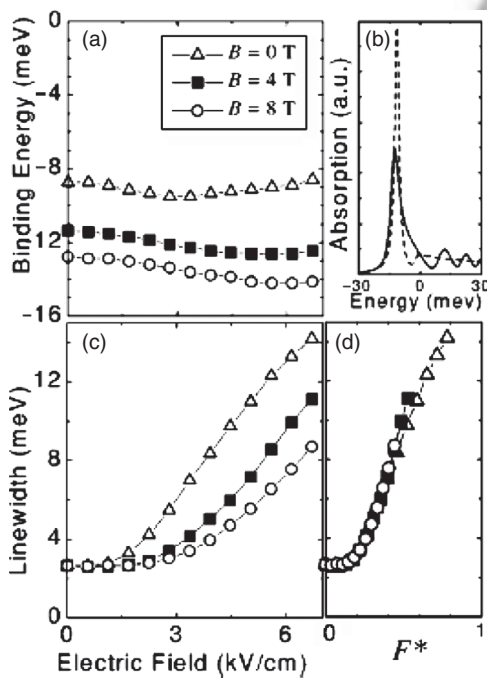


Fig. 22. (a) Magnetoexciton binding energies as functions of the longitudinal electric field. (b) Optical absorption spectra for $B = 4$ T, without (dashed line) and with an applied longitudinal electric field $F = 4.5$ kV/cm (solid line). (c) Linewidths (full width at half maximum) of the fundamental exciton absorption for different magnetic fields as functions of the electric field. (d) The same as in (c) but with the horizontal axis being a scaled electric field. Reprinted with permission from [28], J. R. Madureira et al., *Phys. Rev. B* 66, 075332 (2002). © 2002, American Physical Society.

with respect to the arm well.²⁹ Again, this particularity only affects the effective Coulomb interaction in Eq. (60). We have demonstrated that the dynamical excitation of a nonequilibrium carrier population $n(z, t)$ is an important factor in cancelling out different contributions in the full SBE Eqs. (57) and (58). This is shown in Figure 23 for different intensities of the optical pumping pulse. In Figs. 23(b), (c) and (d) the SBE are solved considering different nonlinear contributions. The local-field contributions tend to produce redshift of the optical absorption peak, whereas the band-gap renormalization yield a blueshift. Inclusion of all terms partially compensates the opposing shifts. Surprisingly the simpler SBE with vanishing nonlinear terms Eq. (61) turns to be a reasonably good approximation as shown in Figure 23(e).

The solutions of the SBE where also used to investigate the dynamical localization of carriers in a quasi-1D superlattice under applied oscillatory (THz) field.³¹ The effect is related to the narrowing of the superlattice minibands for certain values of the field intensity. It was possible to investigate this effect including the interaction between the electron-hole pair (i.e., exciton dynamical localization was investigated), and it was observed that this interaction preserves the dynamical localization effect.

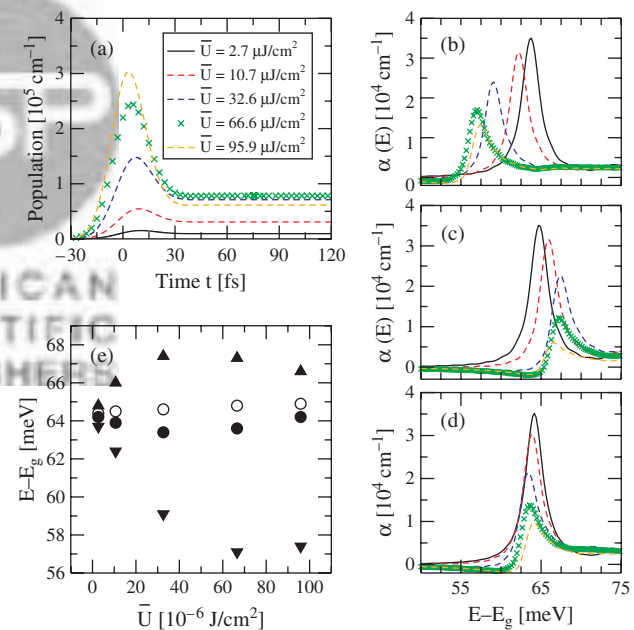


Fig. 23. (a) Carrier density as a function of time for different intensities of the optical pumping pulse. Panels (b–d) show the optical-absorption spectra for different intensities of the pulse. Rest is the same as in panel (a). In (b) we have switched off the local field last term; in (c) we have switched off only the band-gap renormalization term; and in panel (d) we have considered full interactions. Panel (e) shows the exciton peak energy as a function of the intensity of the pumping pulse; triangle down corresponds to panel (b), triangle up corresponds to panel (c), full circle corresponds to panel (d), and empty circle denotes exciton energy switching off band-gap renormalization and local field. Reprinted with permission from [29], J. R. Madureira et al., *Phys. Rev. B* 68, 161301 (2003). © 2003, American Physical Society.

5. CONCLUSIONS

In this review we have presented a numerical method to solve the Schrödinger equation. The method basically performs the time evolution of the wave function. The procedure for the evolution was derived from split-operator methods, applied both for real time as well as imaginary time. The former gives the wave function evolution and the latter gives the eigenvalues and eigenstates of the system. Implementations were made to calculate excited states, carrier–carrier interactions via self-consistent potential, carrier–carrier interaction in many-particle wave functions, periodic and finite-system boundary conditions, and calculation of band structure for periodic systems, all of that in several spatial dimensions. The method was applied to describe several semiconductor systems, treated with the effective-mass approximation. Different physical situations and issues in these systems could be investigated having the method as a support to the knowledge of the quantum states involved. A detailed account of the numerical procedures was given with the intention of diffusing the use of the method to other researchers and students, and the authors would be pleased to give an executable program exemplifying the main procedures.³²

Acknowledgment: The authors are deeply grateful to all their collaborators who share their work and ideas for the improvement of the numerical method and for the applications of the method to the different physical problems discussed in this review. We particularly thank Dr. Justino R. Madureira for his implementations on the problems related to the Semiconductor Bloch Equations. Part of the work presented here was financially supported by the Brazilian agencies FAPESP and CNPq, to which we thank the support. MHD gratefully acknowledges financial support by Dhiminsky ATA and MZM does the same for Liceu Vivere.

References

1. M. D. Feit, J. A. Fleck, Jr., and A. Steiger, *J. Comput. Phys.* **47**, 412 (1982).
2. G. B. Ren and J. M. Rorison, *Phys. Rev. E* **69**, 036705 (2004).
3. Dennis M. Sullivan and D. S. Citrin, *J. Appl. Phys.* **97**, 104305 (2005).
4. O. Stier and D. Bimberg, *Phys. Rev. B* **55**, 7726 (1997).
5. G. Grossi, L. Martinelli, and G. Pastori Parravicini, *Phys. Rev. B* **51**, 13033 (1995).
6. H. Chu and Y.-C. Chang, *Phys. Rev. B* **39**, 10861 (1989).
7. E. R. Davidson, *Comput. Phys.* **7**, 519 (1993).
8. L.-W. Wang, *Phys. Rev. B* **49**, 10154 (1994).
9. S. Glutsch, D. S. Chemla, and F. Bechstedt, *Phys. Rev. B* **54**, 11592 (1996).
10. M. Rieth, W. Schommers, and S. Baskoutas, *Int. J. Mod. Phys. B* **16**, 4081 (2002).
11. M. H. Degani, *Appl. Phys. Lett.* **59**, 57 (1991).
12. E. E. Mendez, F. Agullo-Rueda, and J. M. Hong, *Phys. Rev. Lett.* **60**, 2426 (1988).
13. P. Voisin, J. Bleuse, C. Bouche, S. Gaillard, C. Alibert, and A. Regreny, *Phys. Rev. Lett.* **61**, 1639 (1988).
14. M. H. Degani, *Phys. Rev. B* **44**, 5580 (1991).
15. M. H. Degani, *J. Appl. Phys.* **70**, 4362 (1991).
16. M. H. Degani, G. A. Farias, and F. M. Peeters, *Phys. Rev. B* **72**, 125408 (2005).
17. C. C. Grimes, T. R. Brown, M. L. Burns, and C. L. Zipfel, *Phys. Rev. B* **13**, 140 (1976); E. Collin, W. Bailey, P. Fozooni, P. G. Frayne, P. Glasson, K. Harrabi, M. J. Lea, and G. Papageorgiou, *Phys. Rev. Lett.* **89**, 245301 (2002).
18. M. H. Degani and J. P. Leburton, *Phys. Rev. B* **44**, 10901 (1991).
19. G. A. Farias, M. H. Degani, J. A. K. Freire, J. C. E. Silva, and R. Ferreira, *Phys. Rev. B* **77**, 085316 (2008).
20. M. H. Degani, M. Z. Maialle, G. Medeiros-Ribeiro, and E. Ribeiro, *Phys. Rev. B* **78**, 075322 (2008).
21. M. H. Degani, *Phys. Rev. B* **66**, 233306 (2002).
22. M. J. Calderon, B. Koiller, X. Hu, and S. D. Sarma, *Phys. Rev. Lett.* **96**, 096802 (2006).
23. M. H. Degani, G. A. Farias, and P. F. Farinas, *Appl. Phys. Lett.* **89**, 152109 (2006).
24. M. H. Degani and M. Z. Maialle, *Phys. Rev. B* **75**, 115322 (2007).
25. F. H. L. Koppens, J. A. Folk, J. M. Elzerman, R. Hanson, L. H. Willems van Beveren, I. T. Vink, H. P. Tranitz, W. Wegscheider, L. P. Kouwenhoven, and L. M. K. Vandersypen, *Science* **309**, 1346 (2005).
26. M. Z. Maialle and M. H. Degani, *Phys. Rev. B* **76**, 115302 (2007).
27. M. Scheibner, M. F. Doty, I. V. Ponomarev, A. S. Bracker, E. A. Stinaff, V. L. Korenev, T. L. Reinecke, and D. Gammon, *Phys. Rev. B* **75**, 245318 (2007).
28. J. R. Madureira, M. Z. Maialle, and M. H. Degani, *Phys. Rev. B* **66**, 075332 (2002).
29. J. R. Madureira, M. H. Degani, and M. Z. Maialle, *Phys. Rev. B* **68**, 161301 (2003).
30. J. R. Madureira, M. H. Degani, and M. Z. Maialle, *Appl. Phys. Lett.* **88**, 162108 (2006).
31. J. R. Madureira, P. A. Schulz, and M. Z. Maialle, *Phys. Rev. B* **70**, 033309 (2004).
32. A complete FORTRAN program exemplifying the Stark ladder in superlattices (Sec 3.2) is available by writing to the first author.

Received: 27 February 2009. Accepted: 3 March 2009.